SPACE RESEARCH IN SLOVAKIA

2012 - 2013

SLOVAK ACADEMY OF SCIENCES

COSPAR
SLOVAK NATIONAL COMMITTEE

MAY 2014

ISBN 978-80-89656-07-3
EAN 9788089656073

Contents.

1. EXPERIMENTS FOR MEASUREMENTS IN SPACE

J. Baláž, P. Bobík, K. Kudela, M. Slivka

1.1 Experiment MEP-2 aboard of RADIOASTRON spacecraft

The experiment MEP-2, conducted in the frame of collaboration of Institute of Experimental Physics, Slovak Academy of Sciences (IEP-SAS), Democritus University of Thrace (DUTH), Xanthi, Greece and Space Research Institute of Russian Academy of Sciences (IKI-RAN), Moscow, provides measurements on board of Spectrum-RADIOASTRON satellite over past two years. The MEP-2 operates in space nominally, however, during unfavourable spacecraft orientation some parts of registered data are contaminated by the sunlight. Energetic electron measurements provide the main information. Description of the instrument and a preliminary result on a selected electron event are in [1]. In [2], the data from strong energetic electron flux events measured by MEP-2 during years 2011 and 2012 (near maximum of solar cycle 24) have been compared with those measured by ACE and THEMIS-B satellites in different regions of the Earth's magnetosphere.

1.2 Experiment DOK-M for project RESONANCE

For the experiment DOK-M, developed at IEP-SAS in cooperation with IKI-RAN and DUTH for project RESONANCE, the instrument engineering model DOK-M/EM was constructed and delivered to IKI-RAN in May 2013.

RESONANCE is a magnetospheric space exploration mission conducted by IKI-RAN and dedicated for advanced study of the wave – particle interactions in the Earth's magnetosphere. The Earth's magnetosphere, as natural resonator for many types of electromagnetic waves, is a place where electromagnetic waves efficiently interact with charged energetic particles via cyclotron resonance. The mission consists of four spacecraft in specific Earth orbits, within the same magnetic flux tube for a certain period of time.

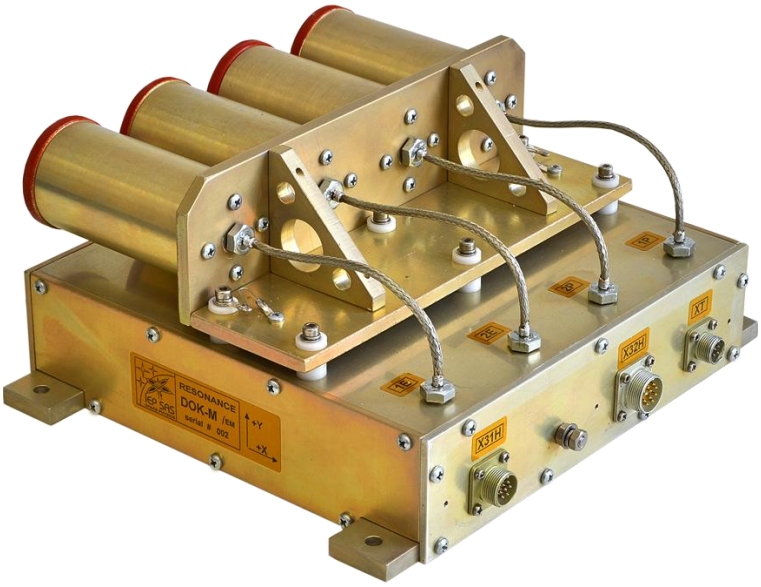

Figure 1.1. Particle spectrometer DOK-M /EM (Engineering Model).

Two models of the DOK-M spectrometer [3] will be installed on board of two satellites of the RESONANCE project.

1.3. Experiment PICAM for mission ESA-BepiColombo

In the frame of collaboration with Space Technology Ireland (STIL) and Institute for Space Research of Austrian Academy of Sciences (IWF-OAW), the Department of Space Physics of IEP-SAS contributes to development and manufacture of the electronic box for planetary ion camera PICAM for ESA mission BepiColombo to planet Mercury.

The electronic box of the flight model PICAM/FM (Fig. 1.2) was delivered to IWF-OAW, Graz in July 2013. The flight-spare model PICAM/FS was delivered to IWF-OAW in April 2014.

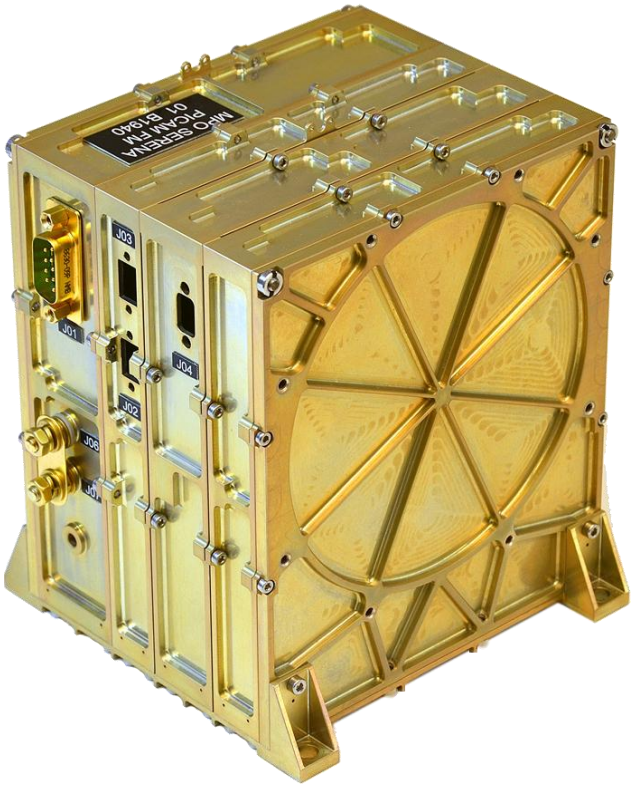

Figure 1.2. The electronic box of the PICAM / FM (flight model).

1.4. Experiment NAIS for Chinese mission MIT (Magnetosphere-Ionosphere-Thermosphere).

In cooperation with Chinese National Space Science Centre (NSSC), Beijing; Space Technology Ireland, Maynooth and Swedish Institute for Space Physics (IRF) in Kiruna; IEP-SAS contributes to development of experiment NAIS (Neutral Atom Imaging System) for Chinese Mesosphere-Ionosphere-Thermosphere (MIT) mission. The high-energy (>30keV) sensor of the experiment, NAIS-H, uses the heritage of neutral atom imager NUADU developed at IEP-SAS for Double Star project, however, with improved angular resolution (Fig.1.3).

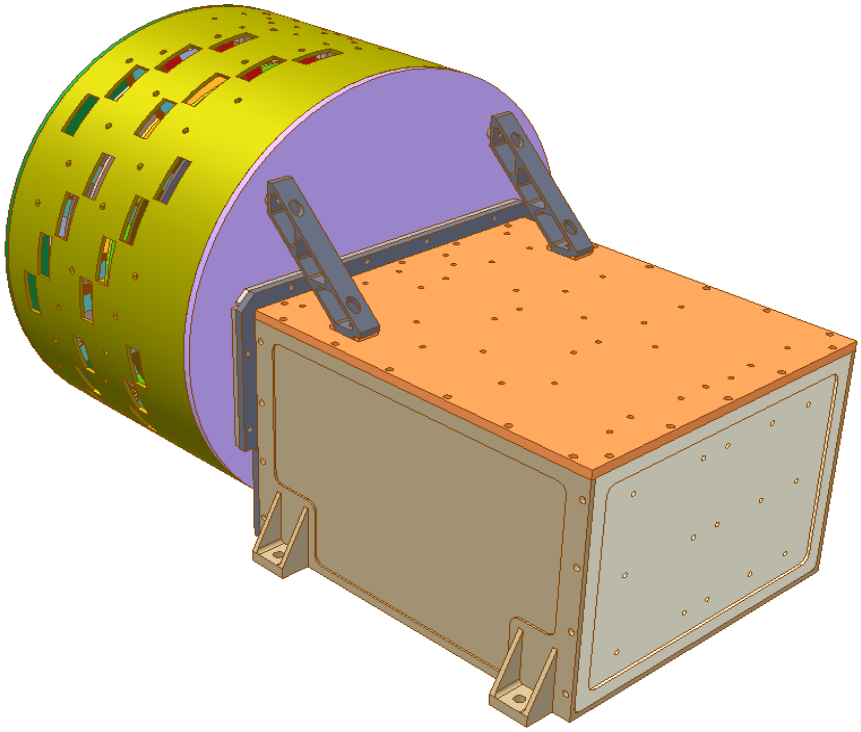

Figure 1.3. Virtual model of neutral atom imager NAIS-H

1.5. Participation of Slovakia in the project JEM-EUSO.

JEM-EUSO (Japanese Experiment Module - Extreme Universe Space Observatory) experiment will search for UHECR (energy above 10^{19} eV) by monitoring UV light produced in their interaction with atmosphere from International Space Station (http://jemeuso.riken.jp/en/index.html). Department of Space Physics IEP-SAS estimated an operational duty cycle for JEM-EUSO experiment along the ISS trajectory (Fig.1.4). Estimation was used for exposure estimation in detector nadir observation mode [4].

UHECR events are very rare and JEM-EUSO experiment will measure during his 3 years or longer stay at International Space Station huge amount of data. Department of Space Physics IEP-SAS provide an analysis of the fake trigger events by pattern recognition methods [5].

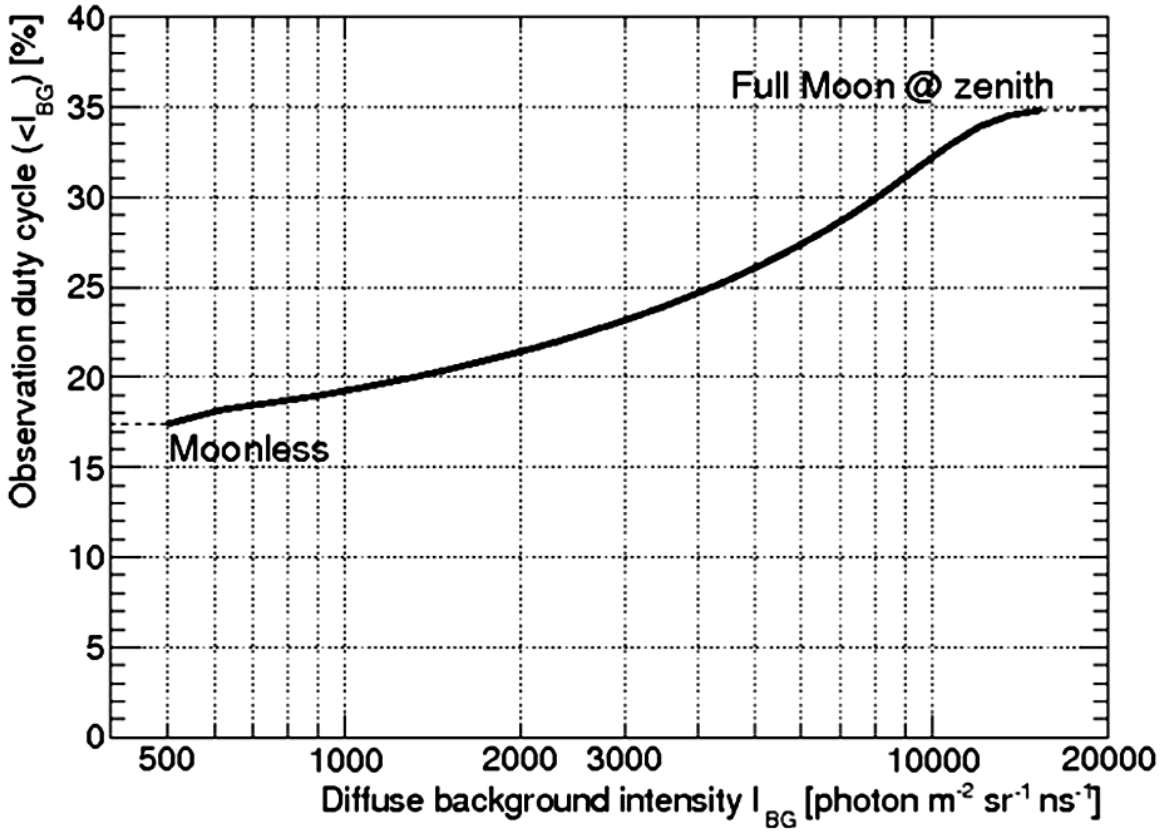

Figure 1.4. Observational duty cycle as a function of the accepted background level. The fraction of time during which background intensity is less than 1500 photons m^{-2} sr^{-1} ns^{-1}.

1.6. Other experiments.

The experiment ASPECT-L is presently under development at IEP-SAS in cooperation with IKI-RAN and DUTH for Moon exploration mission Luna Glob.

Possibilities of the earlier developed experimental device PEEL devoted to measurements of precipitating energetic electrons on the rocket have been discussed in [6].

References:

1. BALÁŽ, J. - GLADYSHEV, V. A. - KUDELA, K. – PETRUKOVICH, A. A. – SARRIS, E. T. – SLIVKA, M. – STRHÁRSKÝ, I. Energetic Particle Measurements Onboard SpectrR with MEP2, Cosmic Research, 2013, Vol. 51, No. 2, pp. 90–95.
2. SLIVKA, M. – KUDELA, K. Multi-Satellite Measurements of Energetic Electron Events during 2011-2012 Period, Proceedings of 20. Conference of Slovak Physicists, Bratislava, 2.9.-5.9.2013, Editor: M.Reiffers, acepted.
3. BALÁŽ, J. – KUDELA, K. – MIZOV, M. – PETRUKOVICH, A. – SARRIS, T. – STRHÁRSKÝ, I. Energetic particle measurements for „RESONANCE“ project, in Multisatellite studies of the inner magnetosphere, Project RESONANCE, Space Res. Inst. RAS, Moscow, ed. M.M. Mogilevsky and I.L. Moiseenko, pp. 98-103, 2012.
4. ADAMS, J. H. Jr. – AHMAD, S. - ALBERT, J. -N. - et al. An evaluation of the exposure in nadir observation of the JEM-EUSO mission, Astroparticle Physics, Volume: 44, Pages: 76-90, DOI: 10.1016/j. astropartphys.2013.01.008, 2013.
5. BIKTEMEROVA, S. - PASTIRČÁK, B. - BERTAINA, M. – BOBIK, P. – FENU, F. – KUDELA, K. – PUTIŠ, M. – STAROŇ, M. – SHINOZAKI, K. Simulations and the analysis of fake trigger events background in JEM-EUSO experiment, id1283, 33rd International Cosmic Ray Conference, 2-9 July, 2013, Rio de Janeiro, Brazil, 2013.
6. BALÁŽ, J. – KUDELA, K. – SARRIS, T. – STRHÁRSKÝ, I. Energetic Electrons Precipitating at High Latitudes: PEEL Data from HotPay-2 Mission, The Open Aerospace Engineering Journal, vol. 6, pp. 20-26, 2013.

2. SPACE PHYSICS, GEOPHYSICS AND ASTRONOMY

I. Dorotovič, K. Kudela,
J. Masarik, A. Ondrášková, M. Revallo, J. Rybák

Activities of institutions in Slovakia related to the space solar physics and X-ray astronomy, interplanetary matter and explorations of the comets, solar wind and its interactions with the Earth's magnetosphere, energetic particles in the magnetosphere and in interplanetary space, atmosphere and ionosphere of the Earth, are continuing in various institutes in Slovakia. The following short survey presents selected activities of the abovementioned directions and the obtained results.

The ***Institute of Experimental Physics, SAS, Košice*** (IEP-SAS, its Department of Space Physics, http://space.saske.sk) in collaboration with the laboratories in abroad continued studies of the dynamics of low energy cosmic rays and of suprathermal cosmic particles, based on measurements in space.

In addition, new results have been obtained from the measurements of ground based neutron monitors, one of them at Lomnický štít (http://neutronmonitor.ta3.sk). A new installation, SEVAN, has been checked in the testing mode in Košice during 2012-2013, and since March 22, 2014 is in operation online at Lomnický štít (http://crd.yerphi.am/Lomnicky_stit_SEVAN_Data). More about the status of ground based measurements as well as about recording system of cosmic ray measurements at IEP-SAS is in [16].

On the occasion of centenary of cosmic ray discovery, a survey of cosmic ray and of suprathermal particle measurements on satellites and on the ground, including the experimental results obtained at IEP-SAS, can be found in [9,11,12]. Observations of high energy gamma rays and neutrons of solar origin on CORONAS-F satellite during several solar flares were analyzed in [10]. Suprathermal particle acceleration observed within the magnetosphere during the experiment on Active satellite is discussed in [1].

Relations between cosmic rays and space weather effects were studied in [7,14]. Some features observed on the ground as irregular and/or quasi-periodic variations of low energy cosmic rays are summarized in [8]. One of the most

important effects with various space weather consequences near Earth as well as on the ground, is arrival of interplanetary shocks. Statistical study analyzing one of the models of the shock arrival to the Earth during solar cycle 23 includes paper [13]. Low energy galactic cosmic rays and solar energetic particles affect the ionosphere. Selected new results on the production rate of ions in the ionosphere due to the high energy particles are included in [17]. Results of statistical study of relations between the geomagnetic storms, Forbush decreases and coronal mass ejections can be found in [15].

The cosmic rays differential intensity inside the heliosphere, for energy below ~30 GeV/nuc, depends on solar activity and interplanetary magnetic field polarity. This variation, termed solar modulation, is described using a 2D (radius and colatitude) Monte Carlo approach for solving the Parker transport equation that includes diffusion, convection, magnetic drift, and adiabatic energy loss. A propagation model of galactic cosmic protons through the heliosphere was implemented using a two-dimensional Monte Carlo approach to determine the differential intensities of protons during solar cycle 23 [2,3]. The model includes the effects due to the variation of solar activity during the propagation of cosmic rays from the boundary of the heliopause down to Earth's position. The simulated spectra were found to be in agreement with those obtained from experimental observations carried out by the BESS, AMS, and PAMELA collaborations.

Cosmic ray positron fraction at energy below ~10 GeV, showing how the particle drift processes could explain different results for AMS-01 and PAMELA. We compare our modulated spectra with observations at Earth, and then make a prediction of the cosmic ray positron fraction for the AMS-02 experiment [6].

The geomagnetic field effect on secondary cosmic ray production is discussed in [4].

Cosmic ray modulation as well as its specific features according to observations by ground based neutron monitors during the recent solar cycle was analyzed in [5].

References:

1. BARANETS, N. - RUZHIN, Y. - EROKHIN, N. - AFONIN, V. - VOJTA, J. - SMILAUER, J. - KUDELA, K. - MATISIN, J. - CIOBANU, M. Acceleration of energetic particles by whistler waves in active space experiment with charged particle beams injection, Adv. Space Res., 49, 5, pp. 859-871, DOI: 10.1016/j.asr.2011.12.001, 2012.
2. BOBIK, P. – BOELLA, G. – BOSCHINI, M. J. – CONSOLANDI, C. - DELLA TORRE, S. – GERVASI, M. – GRANDI, D. – KUDELA, K. - PENSOTTI, S. – RANCOITA, P. G. – TACCONI, M. Systematic Investigation of Solar Modulation of Galactic Protons for Solar Cycle 23 Using a Monte Carlo Approach with Particle Drift Effects and Latitudinal Dependence, The Astrophysical Journal, 745, 2, pp. 132, 2012.
3. BOBIK, P. – BOELLA, G. – BOSCHINI, M. J. – CONSOLANDI, C. - DELLA TORRE, S. – GERVASI, M. – GRANDI, D. – KUDELA, K. - PENSOTTI, S. – RANCOITA, P. G. – ROZZA, D. - TACCONI, M. Latitudinal Dependence of Cosmic Rays Modulation at 1 AU and Interplanetary Magnetic Field Polar Correction, Advances in Astronomy, Article Number: 793072, DOI: 10.1155/2013/793072, 2013.
4. BOBIK, P. – KUDELA, K. - PASTIRCAK, B. - SANTANGELO, A. - BERTAINA, M. - SHINOZAKI, K. - FENU, F. - SZABELSKI, J. - URBAR, J. Distribution of secondary particles intensities over Earth's surface: Effect of the geomagnetic field, Adv. Space Res., 50, 7, pp. 986-996, DOI: 10.1016/j.asr.2012.06.010, 2012.
5. CHOWDHURY, P. - KUDELA, K. - DWIVEDI, B. N. Heliospheric Modulation of Galactic Cosmic Rays During Solar Cycle 23, SOLAR PHYSICS, 286, 2, pp. 577-591, DOI: 10.1007/s11207-013-0262-3, 2013.
6. DELLA TORRE, S. – BOBIK, P. – BOSCHINI, M. J. – CONSOLANDI, C. - GERVASI, M. – GRANDI, D. – KUDELA, K. - PENSOTTI, S. – RANCOITA, P. G. – ROZZA, D. - TACCONI, M. Effects of solar modulation on the cosmic ray positron fraction, Adv. Space Res., 49, 11, pp. 1587-1592, 2012.

7. KUDELA, K. Space weather near Earth and energetic particles: selected results, Journal of Physics Conference Series, 409, Article Number: 012017, DOI: 10.1088/1742-6596/409/1/012017, 2013.
8. KUDELA, K. Variability of Low Energy Cosmic Rays Near Earth, Exploring the Solar Wind, In Lazar, M. (Ed.), ISBN: 978-953-51-0339-4, InTech, DOI: 10.5772/37482, 2012. Available from: http://www.intechopen.com/books/exploring-the-solar-wind/variability-of-low-energy-cosmic-rays-near-earth.
9. KUDELA, K. On Cosmic Rays and Space Weather in the Vicinity of Earth, pp. 177-200, in Homage to the Discovery of Cosmic Rays, the Meson-Muon and Solar Cosmic Rays, Nova Science Publishers, Editor: Jorge A. Perez-Peraza, 2013.
10. KURT, V. - KUDELA, K. - YUSHKOV, B. - GALKIN, V. On the Onset Time of Several SPE/GLE Events: Indications from High-Energy Gamma-Ray and Neutron Measurements by CORONAS-F, Advances in Astronomy, Art. No.: 690921, DOI: 10.1155/2013/690921, 2013.
11. LAZUTIN, L. L. - KUDELA, K. The Space Object of Magnetoplasma: Magnetosphere of Earth, in Interstellar Medium: NewInterstellar Medium: New Research, Nova Science Publishing, pp. 159-195, 2012 .
12. LOGACHEV, Yu I. - LAZUTIN, L. L. - KUDELA, K. Cosmic Ray Investigation in the Stratosphere and Space: Results from Instruments on Russian Satellites and Balloons, Advances in Astronomy, Article Number: 461717, 2013.
13. McKENNA-LAWLOR, S. M. P. - FRY, C. D. - DRYER, M. - HEYNDERICKX, D. - KECSKEMETY, K. - KUDELA, K. - BALAZ, J. A statistical study of the performance of the Hakamada-Akasofu-Fry version 2 numerical model in predicting solar shock arrival times at Earth during different phases of solar cycle 23, Annanles Geophysicae, 30, 2, pp. 405-419, 2012.

14. PAPAILIOU, M. - MAVROMICHALAKI, H. - KUDELA, K. - STETIAROVA, J. - DIMITROVA, S. Cosmic radiation influence on the physiological state of aviators, Natural Hazards, 61, 2, pp. 719-727, DOI: 10.1007/s11069-011-0057-5, 2012.

15. PARNAHAJ, I. – KUDELA, K. – KANCÍROVÁ, M. On Cosmic Ray Decreases, Geomagnetic Storms, and CMEs, in *WDS'13 Proceedings of Contributed Papers: Part II – Physics of Plasmas and Ionized Media* (eds. J. Safrankova and J. Pavlu), Prague, Matfyzpress, pp. 13–19, 2013.

16. STRHÁRSKÝ, I. – LANGER, R. – KUDELA, K. Recording system for cosmic ray measurements at Lomnický štít, presented at 10th European Space Weather Week, November 18-22, 2013, Antwerp, Belgium, Session 13, http://www.stce.be/esww10/contributions/public/posters/Session13/04-KudelaKarel/LomnickyStit-ESWW2013-mid.pdf .

17. VELINOV, P. - ASENOVSKI, S. - KUDELA, K. - LASTOVICKA, J. - MATEEV, L. - MISHEV, A. - TONEV, P. Impact of cosmic rays and solar energetic particles on the Earth's ionosphere and atmosphere, Journal of Space Weather and Space Climate, 3, A14, DOI: 10.1051/swsc/2013036, 2013.

Last 2 years the activities of the ***Department of nuclear physics and biophysics, Faculty of Mathematics, Physics and Informatics, Comenius University, Bratislava,*** have been oriented mainly in the study of cosmic rays and their interaction with material objects.

Neutron capture effects in meteorites and lunar surface samples have been successfully used in the past to study exposure histories and shielding conditions. In recent years, however, it turned out that neutron capture effects produce a nuisance for some of the short-lived radionuclide systems. The most prominent example is the 182Hf-182W system in iron meteorites, for which neutron capture effects lower the 182W/184W ratio, thereby producing too old apparent ages. We thoroughly studied neutron capture effects in iron meteorites, ordinary chondrites, and carbonaceous chondrites, whereas the focus is on iron meteorites. We study in detail the effects responsible for neutron production, neutron transport, and neutron slowing down and find that neutron capture in all studied meteorite types is not, as usually expected, exclusively via thermal neutrons. In contrast, most of the neutron capture in iron meteorites is in the epithermal energy range and there is a significant contribution from epithermal neutron capture even in stony meteorites. Using sophisticated particle spectra and evaluated cross section data files for neutron capture reactions we calculate the neutron capture effects for Sm, Gd, Cd, Pd, Pt, and Os isotopes, which all can serve as neutron-dose proxies, either in stony or in iron meteorites. In addition, we model neutron capture effects in W and Ag isotopes. For W isotopes, the GCR-induced shifts perfectly correlate with Os and Pt isotope shifts, which therefore can be used as neutron-dose proxies and permit a reliable correction. We also found that GCR-induced effects for the 107Pd-107Ag system can be significant and need to be corrected, a result that is in contrast to earlier studies.

Some studies of chemical composition of meteorites were also carried out. Fe-57 Mossbauer spectroscopy was used as an analytical tool in the investigation of iron containing compounds of two meteorites (Rumanova and Kosice) out of total of six which had fallen on Slovak territory. In the magnetic fraction of the iron bearing compounds in the Rumanova meteorite, maghemite, troilite and Fe-Ni alloy were identified. In the non-magnetic fraction silicate

phases were found, such as olivine and pyroxene. The paramagnetic component containing Fe3 + ions corresponds probably to small superparamagnetic particles. The Kosice meteorite was found near the town of Kosice in February 2010. Its magnetic fraction consists of a Fe-Ni alloy with the Mossbauer parameters of the magnetic field corresponding to kamacite alpha-Fe(Ni, Co) and troilite. The non-magnetic part consists of Fe2 + phases such as olivine and pyroxene and traces of a Fe3 + phase. The main difference between these meteorites is their iron oxide content. These kinds of analyses can bring important knowledge about phases and compounds formed in extraterrestrial conditions, which have other features than their terrestrial analogues.

We studied the occurrence of high amplitude, closely correlated, short-lived increases that occurred in four cosmogenic ^{10}Be data records obtained in the Arctic and the Antarctic that we date at 1460 ± 2 AD. They are the only such coincident short-term increases in the past ~600 years, and the combined event has a probability of occurring by chance of ~$2x10^{-5}$. We conclude that they represent additional, short-lived production of ^{10}Be that is unrelated to the ever-present galactic cosmic radiation. The probability that they are of solar origin is low, while their properties are consistent with production by a high-energy gamma ray burst from the relatively close supernova, Vela Junior (RXJ0852.0-4622/ GROJ0852-4642).

On February 15, 2013, after the observation of a brilliant fireball and a spectacular airburst over the southern Ural region (Russia), thousands of stones fell and were rapidly recovered, bringing some extremely fresh material for scientific investigations. We undertook a multi-disciplinary study of a dozen stones of the Chelyabinsk meteorite, including petrographic and microprobe investigations to unravel intrinsic characteristics of this meteorite, and a study of the levels of short and long-lived cosmogenic radionuclides to characterize the initial meteoroid size and exposure age. Petrographic observations, as well as the mineral compositions obtained by electron microprobe analyses, allow confirming the classification of the Chelyabinsk meteorite as an LL5 chondrite. The studied fragments, a few of them being impact melt rocks, contain abundant shock melt veins and melt pockets. It is likely that the catastrophic explosion and fragmentation of the Chelyabinsk meteoroid into thousands of stones was in part determined by the initial state of the meteoroid. The obtained radionuclide

results show a wide range of concentrations of ^{14}C, ^{22}Na, ^{26}Al, ^{54}Mn, ^{57}Co, ^{58}Co, and ^{60}Co, which indicate that the preatmospheric object had a radius >5 m, consistent with other size estimates based on impact geophysics. Considering the observed ^{26}Al activities for the investigated samples and the Monte Carlo simulations we have performed, and taking into account the ^{26}Al half life (0.717 My), the cosmic-ray exposure age of the Chelyabinsk meteorite is estimated to be 1.2 ± 0.2 My. In contrast to the other radionuclides, ^{14}C showed a very large range only consistent with most samples having been exposed to anthropogenic sources of ^{14}C, which we associate with radioactive contamination of the Chelyabinsk region by past nuclear accidents and waste disposal.

The shape of meteorites is one of major factors influencing the production of cosmogenic nuclides. Numerical simulations using LCS particle production and transport codes were done to investigate particle fluxes and production rates of cosmogenic nuclides ^{10}Be, ^{26}Al, ^{53}Mn, and ^{60}Co in meteoroids of spherical, ellipsoidal and cylindrical shapes. The calculations show that fluxes of nuclear active particles and also production rates of cosmogenic nuclides are sensitive to the shape of irradiated parent body.

The structure and stability of the helio nitrogen molecular dication, HeN2+ (2), that is expected to exist in iterstellar space was investigated by means of standard quantum chemical methods based on both single-reference and multi-reference formalisms. Sequences of correlation consistent basis sets are employed to establish convergence with respect to the size and the quality of the single-particle basis set. MRCI and CASPT2 calculations are reported for the HeN2+ (2) ground-state ion which is found to be metastable. The barrier for the transition state of the reaction HeN2+ (2) N+ NHe+ N+ + NHe+ is calculated to be 59.5 kcalsmol(-1). The structure of the transition state NHeN2+ was also determined from calculations using the MRCI and CASPT2 methods.

References:

1. HORNÝ, L. - MACH, P. - MASARIK, J. - HUBAČ, I. - WILSON, S. 2013 Theoretical study of the HeN^{2+}_2 dication. *Molecular Physics* **111 (24)** 3801-3807.
2. LEYA, I. - MASARIK, J. 2013. Thermal neutron capture effects in radioactive and stable nuclide systems. *Meteoritics and Planetary Science* **48 (4)** 665-685.
3. BENO, J. - MASARIK, J. - LEYAR, I. 2013. Neutron production and fluxes in extraterrestrial objects (abstract). *Meteoritics and planetary science* **48** (SI 1) A56.
4. MASARIK, J. - BENO, J. 2013. Numerical simulations of (Kr)-K-81 production rates (abstract). *Meteoritics and planetary science* **48** (SI 1) A57.
5. POVINEC, P. P. - MASARIK, J. - SYKORA, I. - LAUBENSTEIN, M. - BENO, J. - KOVACIK, A. - PORUBCAN, V. Cosmogenic nuclides in Kosice meteorite (abstract). *Meteoritics and planetary science* **48** (SI 1) A288

In the ***Geophysical Institute of the Slovak Academy of Sciences, Bratislava and Hurbanovo***, a number of issues concerning space weather were investigated and ground magnetic field measurements were performed.

Most theoretical studies on space weather prediction were conducted within the framework of the COST Action ES0803 "Developing Space Weather Products and Services in Europe" (http://www.costes0803.noa.gr/) in cooperation with colleagues from the Institute of Geophysics of the ASCR, Prague. This COST Action was born to form an interdisciplinary network between European scientists dealing with different issues of Geospace, as well as warning system developers and operators. Many activities have been carried out by the participants of the COST Action ES0803 that should be shared with the space weather community. In particular, the comprehensive study developed in [4,8,15] presents a summary of results pertaining to the interaction of the solar wind with the magnetosphere and the energy transfer inside the magnetosphere-ionosphere system. The scope of the study is wide since it deals with solar physics, interplanetary physics, magnetospheric physics and aeronomy. The aim of this study is to review those advances made in the framework of the COST Action ES0803 on geomagnetic response to solar and interplanetary disturbances topic that could be useful for the space weather community.

Along with other important topics in [15], an end-to-end forecasting scheme that uses an artificial neural network is focused. Here we show that the forecasting results improve when gathering certain parameters, such as X-ray solar flares (XRAs), Type II and/or Type IV radio emission (RSP) and solar energetic particles enhancements as inputs for the algorithm. Analysis of the particular energetic event types indicates that the degree of their geoeffectiveness depends on their size and on their solar-disc location, see Fig. 2.1. The mere information that a solar XRA event has occurred on the solar disc is insufficient to produce a reliable forecast of geomagnetic disturbances. XRAs of classes B and C were geoeffective in only 2%, XRAs of class M in 8% and XRAs of class X in 33% of cases.

Using the method of artificial neural networks, the geoffectiveness of solar energetic events was studied in [3,5,6]. New models were initiated to involve the solar wind parameters, especially the data concerning the interplanetary magnetic field orientation. In [7,14], a new model to forecast 1-hour lead Dst index was proposed. Our approach was based on artificial neural networks combined with an analytical model of the solar wind-magnetosphere interaction. We evaluated the model for the set of intense geomagnetic storms of the 23-rd solar activity cycle. Furthermore, in [13] we set up a revised model for the geomagnetic activity prediction involving the data on coronal interaction regions (CIRs).

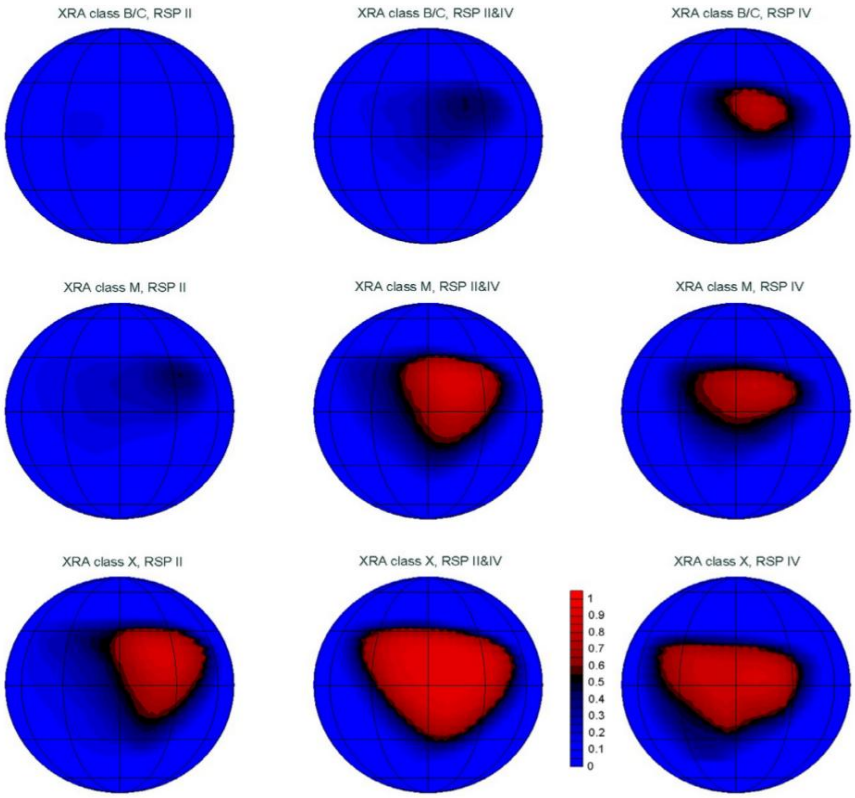

Fig 2.1. Distribution of the probability that the solar events released on a given place on the solar disc produce a geomagnetic response. The areas in which the probability is greater than 50% are shown in red (according to [15]).

Magnetic ground or repeat station surveys are performed to determine the geomagnetic field spatial distribution, which is of great importance for scientific purposes as well as for many applications, for instance the aerial navigation, see [2,9,11,12]. For the information about the geomagnetic field (GMF) distribution

to be complete, the accuracy of the geomagnetic maps needs to be known. It is a custom in the papers dealing with magnetic surveys that the precision of the instruments employed for the measurements are listed there. However, such information is not sufficient to answer the question about the quality of the geomagnetic maps because our experience shows that the spatial variations at a distance of several kilometres often exceed the precisions of the instruments. In paper [9] we proposed a simple method for the evaluation of the accuracy of the GMF distribution maps. We applied it to the maps which were the results of the magnetic ground survey carried out in Slovakia in the 2007.5 epoch. The method is based on the following procedure which is accomplished for each observation point of the magnetic ground survey network: A single point drops out of the data base, then the map is generated in a standard way, whereupon the observed value of the geomagnetic element for the dropped out observation point is compared with the value of the geomagnetic element which is determined from the map. Thus the image of the accuracy of the complete map can be tagged together for the surveyed territory.

The existence of long-acting observatories by itself does not guarantee that their historical magnetograms are available or complete. In the archive of the Hurbanovo Geomagnetic Observatory (acronym HRB; geographical coordinates 47.86 N, 18.19 E), records of the geomagnetic field made on photo paper covering the period between the two World Wars were found for which the values of the baselines are unknown. We studied if a feed-forward neural network with one hidden layer can be used to supplement one-hour means of the geomagnetic elements D, H and Z of observatory HRB, using for this purpose the geomagnetic data of observatories Potsdam, Seddin and Niemegk (all of them being referenced to Niemegk). In [16,17,18], we focused our interest on the first half of the 20-th century. The neural-network model for element D proved to be applicable to substitute for the lost data of the magnetic declination at observatory HRB; however, the usability of the model for both elements H and Z turned out to be limited to a few years close to beginning or end of data gaps. Further we supplemented the time series of annual means of geomagnetic elements D, H and Z at the observatory HRB with the model data.

The observatory HRB performs continuous monitoring and registration of the geomagnetic field components. The one-minute mean values of all components of the geomagnetic field as well as the records acquired with the one-second sampling interval are available. K-indexes characterizing the geomagnetic activity in the middle latitudes are computed regularly. The data are published on the CD-ROMs prepared in the frame of INTERMAGNET. Information about the geomagnetic activity is also published on the web site of the observatory, www.geomag.sk. The level of the geomagnetic activity is reported to public media (TV), too.

The members of the observatory HRB staff regularly perform field measurements at the observation points of the national magnetic repeat station network, which is a part of the European repeat station network. The measurements are coordinated by the MagNetE Group. Measurements of the magnetic declination are performed regularly at selected Slovak airports.

References:

1. DOLINSKÝ, Peter - VALACH, Fridrich - VÁCZYOVÁ, Magdaléna. Accuracy of one-hour means of geomagnetic element H having missing data. In XV-th IAGA workshop on geomagnetic observatory instruments, data acquisition and processing, June 4th-14th, 2012. Boletín ROA no. 2/2012: abstract volume. - Madrid: Ministri de Defensa, 2012, p. 94.
2. DUMA, Gerard - LEICHTER, Barbara - VÁCZYOVÁ, Magdaléna - VALACH, Fridrich - MAGNETE GROUP. Map of magnetic declination in Europe (2006). Vienna : CGMW of UNESCO, 2012
3. HEJDA, Pavel - BOCHNÍČEK, Josef - VALACH, Fridrich - REVALLO, Miloš. Neural network modelling of the impact of solar activity on the Earth environment. In COST action ES0803 "Developing space weather products and services in Europe". Workshop on final results, Prague, 13-14 march 2012: abstract book. - Praha: Ústav fyziky atmosféry AV ČR, 2012, p. 31.

4. SAIZ, Elena - CERRATO, Yolanda - CID, Consuelo - DOBRICA, Verena - HEJDA, Pavel - NENOVSKY, Petko - STAUNING, Peter - BOCHNÍČEK, Josef - DANOV, Dimitar - DEMETRESCU, Crisan - GONZALES, Walter Demetrio - MARIS, Georgeta - TEODOSIEV, Dimitar - VALACH, Fridrich. Geomagnetic response to solar and interplanetary disturbances. In 9th European space weather week, November 5-9, 2012: abstract book & final programme. - Brussel: SWSC, 2012, p. 104.
5. VALACH, Fridrich - REVALLO, Miloš - HEJDA, Pavel - BOCHNÍČEK, Josef. Geomagnetická aktivita pri prevažujúcej južnej orientácii medziplanetárneho magnetického poľa. In: Zborník referátov z 21. celoštátneho slnečného seminára, 18.-22. júna 2012, Stará Turá [elektronický zdroj]. - Hurbanovo : Slovenská ústredná hvezdáreň, 2012, s. [1]. Dostupné na internete: <http://stara.suh.sk/obs/slnsem/21css/25w.pdf>.
6. VALACH, Fridrich - REVALLO, Miloš - HEJDA, Pavel - BOCHNÍČEK, Josef. Geomagnetic activity at predominant south interplanetary magnetic field orientation. In COST action ES0803 "Developing space weather products and services in Europe". Workshop on final results, Prague, 13-14 march 2012: abstract book. - Praha: Ústav fyziky atmosféry AV ČR, 2012, p. 31-32.
7. VALACH, Fridrich - REVALLO, Miloš - HEJDA, Pavel - BOCHNÍČEK, Josef. Modelovanie geomagnetickej búrky metódou umelých neurónových sietí. In Zborník referátov z 21. celoštátneho slnečného seminára, 18.-22. júna 2012, Stará Turá [elektronický zdroj]. - Hurbanovo: Slovenská ústredná hvezdáreň, 2012, s. [1]. Dostupné na internete: <http://stara.suh.sk/obs/slnsem/21css/26w.pdf>.
8. WINTOFT, Peter - BUREŠOVÁ, Dalia - BUSHELL, Andrew - HEJDA, Pavel - INNOCENTI, Maria Elena - LAPENTA, Giovanni - NÚÑEZ, Marlon - PERRONE, Loredana - QAHWAJI, Rami - THOMSON, Alan - TSAGOURI, Ioanna - VALACH, Fridrich - VILJANEN, Ari. Verification of space weather models. In 9th European space weather week, November 5-9, 2012: abstract book & final programme. - Brussel: SWSC, 2012, p. 54.

9. DOLINSKÝ, Peter - VALACH, Fridrich - VÁCZYOVÁ, Magdaléna. Magnetic ground survey of Slovakia for the 2007.5 epoch-accuracy of geomagnetic elements distribution maps. In Contributions to Geophysics and Geodesy, 2013, vol. 43, no. 1, p. 73-80.
10. DOLINSKÝ, Peter - VALACH, Fridrich - VÁCZYOVÁ, Magdaléna. Accuracy of one-hour means of geomagnetic element H having missing data. In Proceedings of the XVth IAGA workshop on geomagnetic observatory instruments, data acquisition, and processing : Bolletín ROA, no. 03/13. - San Fertnando: Ministereo de Defensa, 2013, p. 165-168.
11. DOLINSKÝ, Peter - VÁCZYOVÁ, Magdaléna - VALACH, Fridrich. Effect of artifical disturbances from magnetic dipole sources in the geomagnetic field at the GO Hurbanovo. In 10th Slovak geophysical conference, august 19-21, 2013, Smolenice, Slovak Republic: abstracts [elektronický zdroj]. - Bratislava : Geophysical Institute, Slovak Academy of Sciences, 2013, p. 25.
12. DUMA, Gerard - LEICHTER, Barbara - MAGNETE GROUP - VÁCZYOVÁ, Magdaléna - VALACH, Fridrich. Magnetic declination chart 2006 of Europe - produced by the MagNetE Group. In Annals of Geophysics, 2012, vol. 55, no. 6, p. 1053-1059.
13. HEJDA, Pavel - BOCHNÍČEK, Josef - VALACH, Fridrich - REVALLO, Miloš. The geoeffectivness of solar energetic events" problem revised. In BÖHNEL, Harald. Living on a magnetic planet: 12th scientific assembly, august 26-31, 2013: Abstract volume. - Yucután: Universidad National Autonóma de Mexicó Centro de Geosciencias, 2013, p. 248.
14. REVALLO, Miloš - VALACH, Fridrich - HEJDA, Pavel - BOCHNÍČEK, Josef. Modeling of intense geomagnetic storms by using an empirical model and artificial neural networks. In 10th Slovak geophysical conference, august 19-21, 2013, Smolenice, Slovak republic: abstracts [elektronický zdroj]. - Bratislava: Geophysical Institute, Slovak Academy of Sciences, 2013, p. 60.

15. SAIZ, Elena - CERRATO, Yolanda - CID, Consuelo - DOBRICA, Verena - HEJDA, Pavel - NENOVSKI, Petko - STAUNING, Peter - BOCHNÍČEK, Josef - DANOV, Dimitar - DEMETRESCU, Crisan - GONZALES, Walter Demetrio - MARIS, Georgeta - TEODOSIEV, Dimitar - VALACH, Fridrich. Geomagnetic response to solar and interplanetary disturbances. In Journal of Space Weather and Space Climate, 2013, vol. 3, p. A26.

16. VALACH, Fridrich - VÁCZYOVÁ, Magdaléna - DOLINSKÝ, Peter - VAJKAI, Melinda. The historical data of the Hurbanovo Geomagnetic Observatory reconstructed by means of neural networks. In 10th Slovak geophysical conference, august 19-21, 2013, Smolenice, Slovak Republic: abstracts [elektronický zdroj]. - Bratislava: Geophysical Institute, Slovak Academy of Sciences, 2013, p. 78.

17. VALACH, Fridrich - VÁCZYOVÁ, Magdaléna - DOLINSKÝ, Peter - VAJKAI, Melinda. Substitution for lost one-hour means of the geomagnetic elements for the first half of the 20-th century at the Hurbanovo Geomagnetic Observatory by means of neural networks. In Contributions to Geophysics and Geodesy, 2013, vol. 43, no. 2, p. 128-140.

18. VALACH, Fridrich - VÁCZYOVÁ, Magdaléna - DOLINSKÝ, Peter - VAJKAI, Melinda. Substitution for lost one-hour means of the geomagnetic elements for the first half of the 20-th century at the Hurbanovo Geomagnetic Observatory by means of neural networks. In Program and book abstracts. - Praha: Institute of Geophysics of the ASCR, 2013, p. 14.

In the ***Department of Astronomy, Physics of the Earth and Meteorology, Faculty of Mathematics, Physics and Informatics, Comenius University, Bratislava,*** the study of Schuman resonances (SR) continued. The more precise determination of instantaneous peak frequency of SR modes, especially based on relatively short signal sequences, seems to be important for detailed analysis of SR modal frequencies variations. Contrary to commonly used method of obtaining modal frequencies by Lorentzian fitting of DFT spectra, the attempt was made to employ the complex demodulation method in iterated form. The results for SR signals contaminated with low-frequency noise and hum in various degree as well as the comparison with standard method are presented. Real signals of vertical electric field component picked up at the Astronomical and Geophysical Observatory of Comenius University at Modra, Slovakia, were the primary sources.

References:

1. ONDRÁŠKOVÁ, Adriena - ŠEVČÍK, Sebastián. The determination of Schumann resonance mode frequencies using iterative procedure of complex demodulation. In Contributions to Geophysics and Geodesy, 2013, vol. 43, no. 4, p. 305-326.

In the ***Slovak Central Observatory*** in Hurbanovo (http://www.suh.sk), a number of activities related to space research were performed. We observed sunspots (the Wolf number data were submitted to the SIDC in Brussels, Belgium and to the SONNE Netz in Germany) and prominences (images are published at the website of the Observatory). We performed also spectrographic observations of the solar spectrum (variations of selected spectral lines during a solar activity cycle) using a horizontal solar telescope with spectrograph, we registered solar radio bursts using a solar radio spectrometer CALLISTO and impact of solar flares on the Earth's ionosphere using SID monitors. The research activities comprise study of the:

- rotation of the solar corona,
- asymmetry of the north and south hemispheric solar activity,
- oscillations of the cross-sectional area and the intensity of magnetic waveguides located in the lower solar atmosphere,
- time-latitude distribution of prominences,
- impact of the solar activity on tree growth.

We published at the website of the SCO data on the modified coronal index (MCI) and the modified homogeneous data set (MHDS) of coronal intensities based on satellite EUV measurements as a repacement of ground-based coronagraphic observations at Lomnický Štít.

The solar radio spectroheliogram CALLISTO and the SuperSID monitor were installed in the SCO in 2011 in the frame of the instrument deployment program of the International Space Weather Initiative (ISWI - http://iswi-secretariat.org) where one researcher from the SCO is also the national ISWI coordinator for the Slovak Republic. Preliminary results are published in [1, 2].

In [3] the differential rotation of the solar corona using the images taken at a 9.4 nm wavelength by the AIA 094 instrument on board the *Solar Dynamics Observatory* (SDO) satellite. Based on the analysis of the results derived above we infer that the tracer method (either interactive or manual) is sufficiently precise, hence the obtained values of the rotational speed are reliable. However, the method is laborious and becomes practically unworkable on a large number

of images. Therefore, in the future we would like to focus on automated image processing while preserving the precision of the method used thus far. To determine the rotational speed we plan to use the method of cross-correlation analysis using the images of the AIA instrument on board the SDO satellite. Jet stream is a layer where the rotational speed of the solar surface is higher than the average value. This layer is also an indicator of hypothetical processes that take place under the solar surface, and its location (heliographic latitude) is probably related with phase of the solar activity cycle. We are trying in to determine its position by using a series of images obtained from the AIA instrument onboard the SDO satellite using a two-phase method. The first phase [4] includes the estimation of the rotational speed in a big range of latitudes (Fig. 2.2) and the second phase [4, 5, 8] uses a hybrid algorithm combining PSO (Particle Swarm Optimization) and Snake algorithms for detecting, tracking and determining the rotation of coronal bright points (CBPs). The software tool has been developed in collaboration with UNINOVA-CA3, Caparica (Portugal).

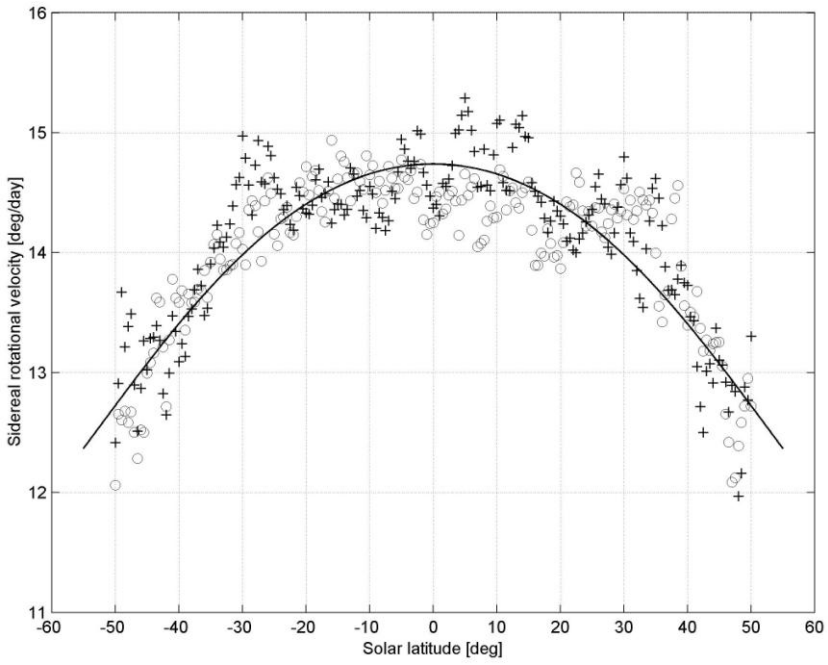

Figure 2.2. Sidereal rotational velocity of the solar corona as a function of solar latitude.
o - *average velocity at a particular latitude from 456 measurements on 3 and 4 September 2010;* + - *average velocity at a particular latitude from 536 measurements on 5 and 6 September 2010.*
Approximation: sidereal angular velocity of coronal rotation $\omega = 14.739 - 2.73 \sin^2 b - 1.2 \sin^4 b$.

Ca II K3 spectroheliograms registered in the Observatório Astronómico da Universidade de Coimbra (Portugal) were used to derive the surface area of bright chromospheric plages. Evolution of the area of and the corresponding north-south (N-S) asymmetry of this area, as measured in the in the period of 1975 – 2008, was studied in [6]. A comparison and cross-correlation with the N-S asymmetries found for the sunspots and coronal green line brightness is added. The highest correlation was found between the Ca-plages and the SIDC sunspot number N-S asymmetries (with maximum CC = +0.69), while the correlation between the Ca-plages and the CGLB N-S asymmetries was in individual latitudinal zones from CC = +0.27 up to CC = +0.48 (the CGLB was considered separately for four chosen zones of solar latitude).

By focussing on the oscillations of the cross-sectional area and the total intensity of magnetic waveguides located in the lower solar atmosphere, we aimed in [10] to detect and identify magnetohydrodynamic (MHD) sausage waves. Two sunspots and one pore (with a light bridge) were chosen as examples of MHD waveguides in the lower solar atmosphere. The presence of fast and slow MHD sausage waves has been detected in three different magnetic waveguides in the solar photosphere. The waveguides display a range of periods from 4 to 65 min. These structures display in-phase behaviour between the area and intensity, presenting mounting evidence for sausage modes within these waveguides. The detected periods point towards standing oscillations.

It seems that prominences occur randomly across the surface of the Sun. This applies only to heliographic latitudes of ±40°, and even this is not valid everywhere. In higher latitudes is clearly observable the so-called polar branch of prominences (Fig. 2.3 and 2.4). It is an interesting indicator of the magnetic polarity reversal. It would be appropriate for these purposes to consolidate the method of processing of observations and to publish them electronically in a standardized form by one institute. In [11] only observations from one observatory, thus there are big gaps caused by the weather. In spite of this fact we assume that such observations can also contribute to reveal a mechanism of solar cycle which is not well understood, yet.

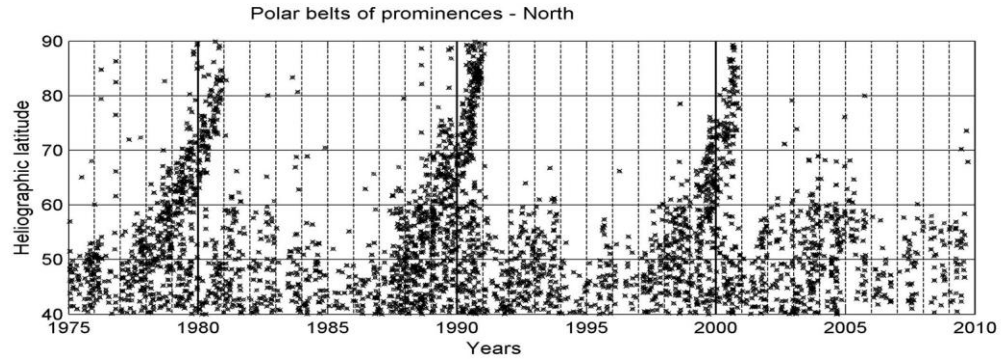

Figure 2.3. Polar branches of prominences near the North Pole of the Sun.

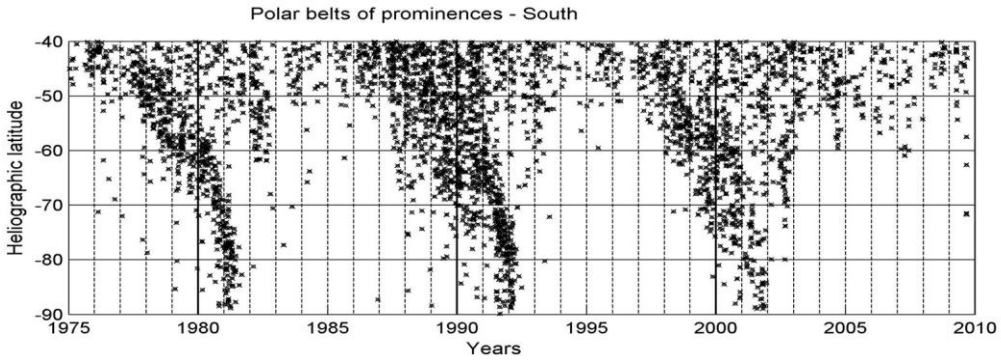

Figure 2.4. Polar branches of prominences near the South Pole of the Sun.

In [12] we focused on the analysis of data for the ring width of two pine tree species: samples of six maritime pines (*Pinus pinaster*), grown in the north of Portugal, and one sample of Scots pine (*Pinus sylvestris*), grown in the south of Slovakia. A negative impact of solar activity (SA) represented by the sunspot number (SSN) was observed on the growth of these pine trees with particularly strong impact in the case of the maritime pines. The width of the annual rings was generally smaller in the years of maximum SA; furthermore, it was found that it is latewood width (LWW) that is affected whereas earlywood width (EWW) is not affected (Fig. 2.5); as a corollary, the percentage of latewood also shows a significative negative correlation with SA.

The Astronomical Institute of the Slovak Academy of Sciences has published the intensities, recalibrated with respect to a common intensity scale, of the 530.3 nm (Fe XIV) green coronal line observed at ground-based stations up to the year 2008. The name of this publication is Homogeneous Data Set (HDS). We have developed a method that allows one to successfully substitute the ground-based observations by satellite observations and, thus, continue with

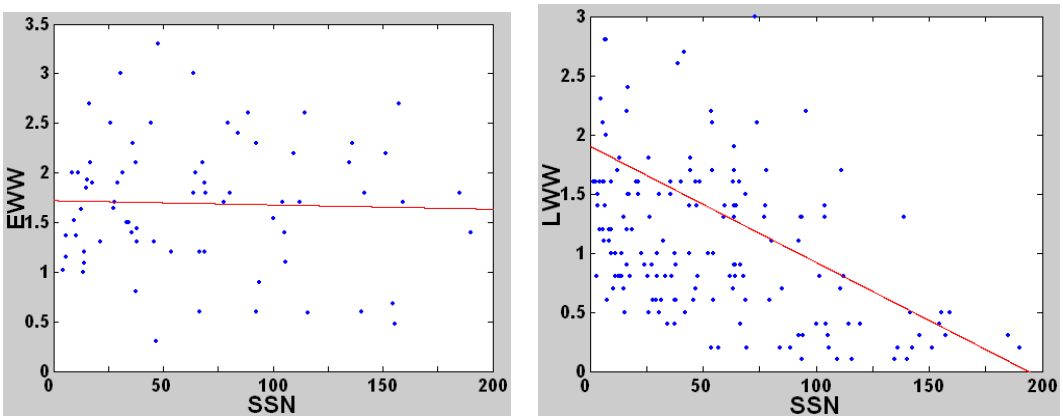

Figure 2.5. Bivariate fit of the EWW (left panel) and the LWW (right panel), respectively, of the maritime pine by the solar (sunspot) activity (yearly SSN).

the publication of the HDS [13]. For this purpose, the observations of the *Extreme-ultraviolet Imaging Telescope* (EIT), onboard the *Solar and Heliospheric Observatory* (SOHO) satellite, were exploited. Among other data the EIT instrument provides almost daily 28.4 nm (Fe XV) emission-line snapshots of the corona. The Fe XIV and Fe XV data (4051 observation days) taken in the period 1996 - 2008 have been compared and good agreement was found. The method to obtain the individual data for the HDS follows from the correlation analysis described in this article. The resulting data, now under the name of Modified Homogeneous Data Set (MHDS), are identical up to 1996 to those in the HDS. The MHDS can be used further for studies of the coronal solar activity and its cycle. These data are available at the website of the SCO.

The Slovak Central Observatory organised in the year 2012 the National Solar Physics Meeting with participation from abroad. The goal of the Meeting is to present new results of solar physics and from the field of the Sun-Earth connections, to provide overview of present status in selected fields of solar physics and geophysics. A separate space will be devoted to the presentation of research results of undergraduate and PhD students of university and academic departments and also to results of scientific and popularisation activities of Astronomical Observatories in the Slovak Republic and the Czech Republic. Invited talks, short contributions and posters should cover the following fields: physical phenomena in the solar atmosphere, solar activity, total solar eclipses, space weather and geoactivity.

References:

1. DOROTOVIČ I. - PINTÉR T. (2012). Slnečný rádiový spektrometer CALLISTO v Hurbanove - prvé výsledky. In Zborník referátov z 21. celoštátneho slnečného seminára, 18. - 22. júna 2012, Stará Turá [elektronický zdroj] - Hurbanovo: Slovenská ústredná hvezdáreň, I. Dorotovič (ed.), 28.pdf. (in Slovak)
2. DOROTOVIČ I. - PINTÉR T. (2012). SID monitoring na Slovensku. In Zborník referátov z 21. celoštátneho slnečného seminára, 18. – 22. júna 2012, Stará Turá [elektronický zdroj] - Hurbanovo: Slovenská ústredná hvezdáreň, I. Dorotovič (ed.), 29.pdf. (in Slovak)
3. LORENC M. - RYBANSKÝ M. - DOROTOVIČ I. (2012). On Rotation of the Solar Corona, Solar Physics, Volume 281, Issue 2, 611-619. DOI: 10.1007/s11207-012-0105-7.
4. RYBANSKÝ M. - DOROTOVIČ I. - LORENC M. - SHAHAMATNIA E. - RIBEIRO R.A. – FONSECA J.M. (2014). Hľadanie jet streamu. In Zborník referátov z 21. celoštátneho slnečného seminára, 18. – 22. júna 2012, Stará Turá [elektronický zdroj] - Hurbanovo: Slovenská ústredná hvezdáreň, I. Dorotovič (ed.), 19.pdf. (in Slovak)
5. SHAHAMATNIA E. - DOROTOVIČ I. - RIBEIRO R.A. - FONSECA J.M. (2012). Towards an automatic sunspot tracking: Swarm intelligence and snake model hybrid. In ESA Acta Futura, Volume 5, 153-161. DOI: 10.2420/AF05.2012.153.
6. DOROTOVIČ I. - RYBÁK J. - GARCIA A. - JOURNOUD P. (2012). Severo-južná asymetria oblastí Ca II K3 určená zo spektroheliogramov OAUC - II: 1975 – 2008. In Zborník referátov z 21. celoštátneho slnečného seminára, 18. – 22. júna 2012, Stará Turá [elektronický zdroj] - Hurbanovo: Slovenská ústredná hvezdáreň, I. Dorotovič (ed.), 10.pdf. (in Slovak)
7. LORENC M. - DOROTOVIČ I. - RYBANSKÝ M. (2012). Variácie emisných čiar ultrafialovej slnečnej koróny a koronálny index. In Zborník referátov z 21. celoštátneho slnečného seminára, 18. – 22. júna 2012, Stará Turá [elektronický zdroj] - Hurbanovo: Slovenská ústredná hvezdáreň, I. Dorotovič (ed.), 17.pdf. (in Slovak)

8. DOROTOVIČ I. - SHAHAMATNIA E. - LORENC M. - RYBANSKÝ M. - RIBEIRO R.A. - FONSECA J.M. (2014). Sunspots and Coronal Bright Points Tracking using a Hybrid Algorithm of PSO and Active Contour Model, Sun and Geosphere, Volume 9, No. 2, 81-84.
9. DOROTOVIČ I. - PINTÉR T. (2014). Solar Radio Spectrometer CALLISTO in Hurbanovo - first results, Sun and Geosphere, Volume 9, No. 2, 105-107.
10. DOROTOVIČ I. - ERDÉLYI R. - FREIJ N. - KARLOVSKÝ V. - MÁRQUEZ I. (2014). Standing sausage waves in photospheric magnetic waveguides, Astronomy and Astrophysics, Volume 563, A12. doi: 10.1051/0004-6361/201220542.
11. PINTÉR T. - RYBANSKÝ M. - DOROTOVIČ I. (2014). The polar belts of prominence occurence as an indicator of the solar magnetic field reversal. In 'Nature of Prominences and their role in Space Weather', Proceedings of the International Astronomical Union, IAU Symposium, B. Schmieder, J.-M. Malherbe, and S. Wu (eds.), Volume 300, 456-457. DOI: 10.1017/S1743921313011538.
12. DOROTOVIČ I. - LOUZADA J.L. - RODRIGUES J.C. - KARLOVSKÝ V. (2014). Impact of Solar Activity on the Growth of Pine Trees – Case Study, European Journal of Forest Research, Published online in February 2014. DOI: 10.1007/s10342-014-0792-8.

The activities of ***the Astronomical Institute of the Slovak Academy of Sciences (AISAS)***, Tatranská Lomnica (www.astro.sk), related to COSPAR, were devoted to the research in solar and stellar physics using different satellite observations, mainly in the UV, XUV and X-ray spectral regions. Stellar data of the IUE, FUSE, INTEGRAL, Kepler satellites, and the HST were used for research of various variable stars [1]. Data of the current SOHO mission, Hinode, SDO, TRACE and RHESSI satellites and previous satellites of the NOAA and GOES series were used for solar research [2, 3]. Hereby we present some examples of the results obtained by the AISAS staff, an information on an education activity of the AISAS and an information on the WAMIS project cooperation.

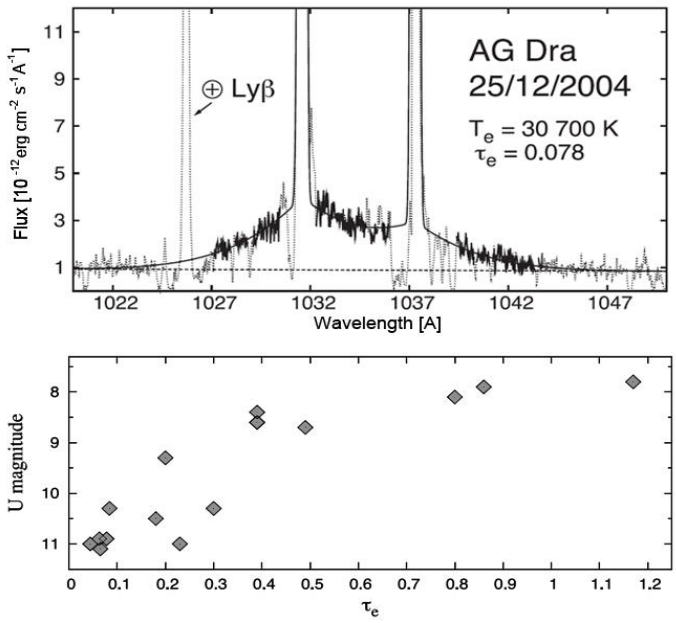

Figure 2.6. The top panel shows an example of the observed (dotted line) and modelled profile (thick line) of the wide wings of the line OVI 1032, 1038 Å in the symbiotic star AG Dra. The bottom panel depicts a relationship between the electron optical depth and the U magnitude as the indicator of the activity level in AG Dra.

Within the research of the stellar astrophysics, the data carried out with the space observatories, the Far Ultraviolet Spectroscopic Explorer (FUSE) and International Ultraviolet Explorer (IUE) were used to model the very shallow and wide wings of the strongest emission lines OVI 1032, 1038 Å and HeII 1640 Å, observed in the spectra of symbiotic stars Z And, AG Dra and V1016

Cyg during different phases of activity. Theoretical profiles of these lines were calculated for the case of the light scattering on free electrons, the so-called Thomson scattering. By this way we determined mean values of electron optical depth and electron temperature, which characterize scattering region represented by symbiotic nebula. We found that physical properties of the nebula are directly connected with changes of the hot component of the binary, which results in relationship between these two parameters and phases of the activity. This relationship can be used to determine more precisely mass loss rate from the hot star, which is very important in understanding the nature of the symbiotic stars outbursts (see Fig. 2.6). [1]

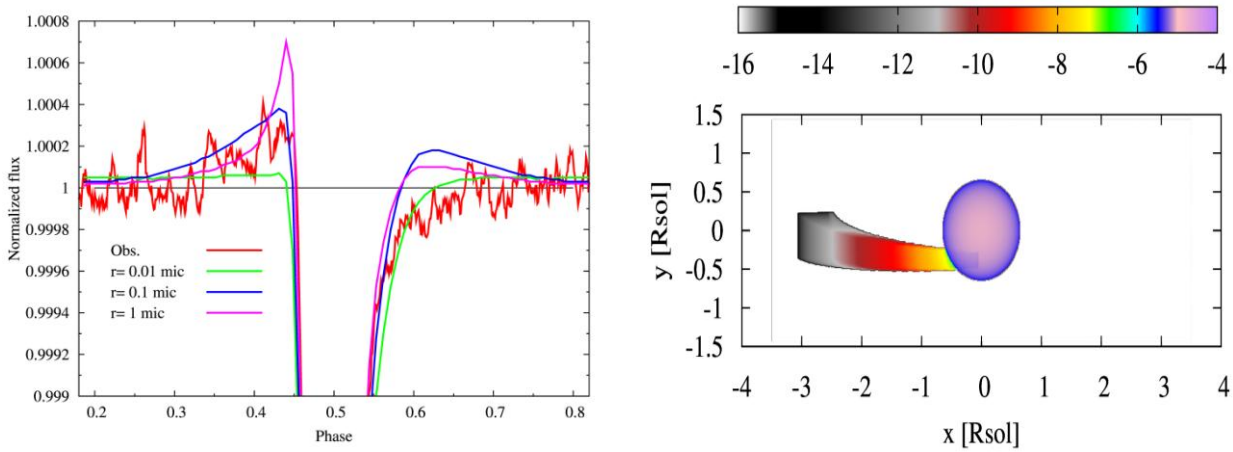

Figure 2.7. Left panel: Effect of the particle size on the light curve for the Kepler short-cadence observations calculated for pyroxene grains and A2 = −20. Right panel: 2D image (intensity logarithm, Iv, in erg cm−2 s−1 Hz−1) of the planet with a comet like tail during the transit. The intensity of the tail rapidly decreases because of a decrease in the dust density and forward scattering. Note also the optically thin absorption on the limb-darkened stellar disk.

The light curve of KIC12557548b - an extrasolat planet with a comet like tail was analysed using long- and short-cadence Kepler observations from the first 14 quarters. The orbital period of the planet was improved. We prove that the peculiar light curve agrees with the idea of a planet with a comet-like tail. The light curve has a prominent pre-transit brightening (Fig. 2.7) and a less prominent post-transit brightening. Both are caused by the forward scattering and are a strong function of the particle size. This feature enabled us to estimate

a typical particle size (radius) in the dust tail of about 0.1-1 micron. However, there is an indication that the particle size changes (decreases) along the tail. The dust density in the tail is a steep decreasing function of the distance from the planet, which indicates a significant tail destruction caused by the star-planet interaction. We revealed interesting periodic long-term evolution of the tail on a time scale of about 1.3 years and also argue that the "planet" does not show a uniform behaviour, but may have at least two constituents. This exoplanet's tail evolution may find an analogy in the comet tail disconnection events caused by the magnetic/coronal activity of the Sun while the light curve with pre-transit brightening is analogous to the light curve of Epsilon Aur and AZ Cas with mid-eclipse brightening and forward scattering playing a significant role in such eclipsing systems. [2]

We combined high-resolution SoHO/MDI magnetograms with TRACE observations taken in the 1216 Å channel to analyze the temporal evolution of an emerging small-scale magnetic loop and its traces in the chromosphere. We find signatures of flux emergence close to the edge of a supergranular network boundary located at disk center. The new emerging flux appeared first in the magnetograms in form of an asymmetric bipolar element, i.e., the patch with negative polarity is roughly twice as weak as the corresponding patch with opposite polarity (Fig. 2.8.). The average values of magnetic flux and magnetic flux densities reached 1.6×10^{18} Mx, -8.5×10^{17} Mx, and 55 Mx/cm^2, -30 Mx/cm^2, respectively. The spatial distance between the opposite polarity patches of the emerged feature increased from about 2.5 arcsec to 5.0 arcsec during the lifetime of the loop, which was 36 min. The chromospheric response to the emerged magnetic dipole occurred ~9 min later than in the photospheric magnetograms. It consisted of a quasi-periodic sequence of time-localized brightenings visible in the 1216 Å TRACE channel for ~14 min that were co-spatial with the axis connecting the two patches of opposite magnetic polarity. We identify the observed event as a small-scale magnetic loop emerging at photospheric layers that subsequently rose to the chromosphere. We discuss the possibility that the fluctuations detected in the chromospheric emission probably reflect magneticfield oscillations which propagate to the chromosphere in the form of waves. [3]

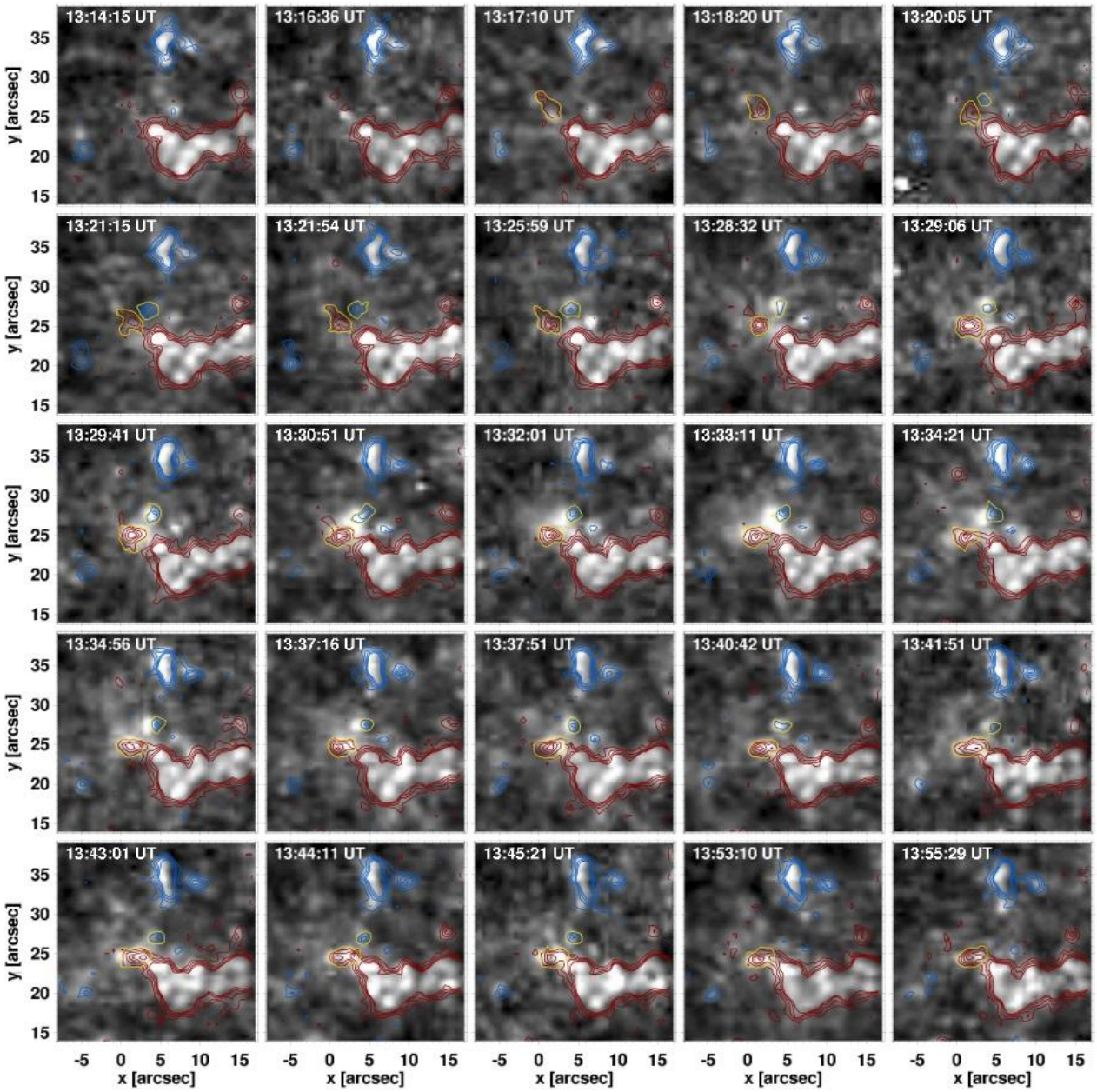

Figure 2.8. Temporal evolution of the emerging magnetic dipole. Background images have been taken in the TRACE 1216 Å channel. The superimposed contours represent the magnetic signal detected in the SoHO/MDI data with red (blue) contours referring to positive (negative) magnetic polarity. The yellow contours mark the emerging loop.

The Astronomical Institute organised in the year 2013 the lecture course – solar Spectro-polarimetry - given for the undergraduate and PhD students from Slovakia by Dr. Horst Balthasar of the AIP – Leibnitz Institute for Astrophysics Potsdam (Germany) on June 3-7, 2013 at AISAS at Tatranska Lomnica. The

course of lectures provided insights on the physical background, observational possibilities and numerical analysis of spectro-polarimetric measurements which provide a very important tool to study properties of solar magnetic fields. The course started with the theoretical background of polarized light and the magnetic sensitivity of spectral lines. In the second part, optical elements for polarimetry were presented, and it was demonstrated how they can be combined to a polarimeter. In the third part, we were dealing with spectro-polarimetric observations at modern solar telescopes. The numerical analysis of the data has been discussed in the last part. In total 15 students took part in the course. More details about the course of lectures can be found at the dedicated web page - http://www.astro.sk/~gomory/SPECTRO/spectro.

In 2013 AISAS has become involved also in the proposal which has been submitted for consideration of an award by NASA (Proposal Number: 13-HTIDS13_2-0018). The portal called "Waves and Magnetism in the Solar Atmosphere (WAMIS)" is led by Yuan-Kuen Ko, Naval Research Lab, Washington, USA (PI), and its AISAS part by J. Rybak. The team is waiting for the agency decision. The project is a long duration balloon based 20cm aperture coronagraph designed to obtain continuous measurements over at least a week of the strength and direction of coronal magnetic fields within a large field-of-view at the spatial and temporal resolutions required to address several outstanding problems in coronal physics. The WAMIS investigation, comprising a balloon-borne infra-red coronagraph and polarimeter to observe forbidden transitions in Fe XIII and HeI, should enable breakthrough science and enhance the value of data collected by other observatories on the ground (e.g. ATST, FASR, SOLIS, COSMO) and in space (e.g. Hinode, STEREO, SDO, TRACE, GOES, SOHO and IRIS), and will advance the technology for a future orbital missions.

Besides of this, the AISAS staff was involved (or leading) in the last two years in total 5 coordinated observing campaigns focused on observations of several aspects of the solar activity. The integral part of the campaigns were also measurements performed by the space-born instruments on different satellites, e.g. SUMER/SoHO, EIS/Hinode. The measurements were coordinated with the

ground-based instruments including the AISAS owned CoMP-S instrument at the Lomnicky Peak Observatory.

References:

1. SEKERÁŠ, Matej - SKOPAL, Augustin. Electron optical depths and temepratures of symbiotic nebulae from Thomson scattering. In *Monthly Notices of the Royal Astronomical Society*. 2012, vol. 427, p. 979-987.
2. GÖMÖRY, Peter - BALTHASAR, Horst - PUSCHMANN, Klaus. Evidence of quiet-Sun chromospheric activity related to an emerging small-scale magnetic loop. In *Astronomy and Astrophysics*, 2013, vol. 556, article no. A7, p. 1-6.
3. BUDAJ, Ján Light-curve analysis of KIC 12557548b: an extrasolar planet with a comet-like tail. In *Astronomy and Astrophysics* 2013, vol. 557, A72.
4. SCHWARTZ, Pavol - SCHMIEDER, Brigitte - HEINZEL, Petr - KOTRČ, Pavel. Study of an extended EUV filament using SOHO/SUMMER observations of the hydrogen Lyman lines: II. Lyman alpha line observed during a multi-wavelength campaign. In *Solar Physics*, 2012, vol. 281, p. 707-72.

3. MATERIALS RESEARCH IN SPACE

J. Lapin, A. Klimová, Z. Gabalcová

Material research activities in space of the ***Institute of Materials and Machine Mechanics of the Slovak Academy of Sciences*** (IMMS SAS) in the period 2012-2013 were focused on the international project with ESA entitled "Gravity dependence of CET in peritectic TiAl alloys (acronym GRADECET)". The international consortium of the project consists of six partners: Access e.V. - project coordinator (Aachen, Germany), Ecole des Mines de Nancy (Institut Jean Lamour, SI2M, Nancy, France), Deutsches Zentrum für Luft- und Raumfahrt (Institut für Materialphysik im Weltraum, Köln, Germany), Dublin Institute of Technology (Dublin, Ireland), Research Institute for Solid State Physics and Optics (Hungarian Academy of Sciences, Budapest, Hungary) and Institute of Materials and Machine Mechanics (Slovak Academy of Sciences, Bratislava, Slovak Republic). Project GRADECET is divided into three distinguished phases: (i) extensive ground based preparatory phase aiming at producing all necessary data and technical solutions for space mission, (ii) space mission using sounding rocket MAXUS and (iii) ground based evaluation of samples prepared at microgravity and hypergravity conditions. Four peritectic TiAl base alloys with nominal compositions Ti-43.5Al-5Nb-0.2C-0.2B, Ti-44.5Al-5Nb-0.2C-0.2B, Ti-46.5Al-5Nb-0.2C-0.2B and Ti-47Al-5Nb-0.2C-0.2B (at.%) are evaluated in the frame of the project. These alloys are candidates for near net shape casting of light-weight structural components, like aero-engine blades and turbocharger wheels for automotive engines.

One possible event in casting of TiAl alloys is columnar to equiaxed transition (CET). The CET occurs during columnar growth when equiaxed grains begin to form, grow, and subsequently stop the columnar growth. Normally either a columnar or equiaxed grain structure is desired in industry applications, so that consistent mechanical properties are achieved throughout the casting. During solidification, the CET leads to a change of the grain structure within castings and hence to a change of their mechanical properties. For most TiAl castings, solidification with equiaxed grains is targeted, aiming to

achieve isotropic properties throughout the cast component. Therefore, understanding the CET in microgravity, ground based gravity and hypergravity conditions is of a great importance from fundamental and industrial point of view to accelerate further development and industrial applications of these light weight high-temperature structural alloys. The participation of IMMM SAS in the project is financially supported by the Slovak Academy of Sciences (SAS) in the frame of international cooperation of SAS with ESA.

Microgravity solidification experiments offer a unique opportunity to minimise the effects of convection (thermal and solutal) and subsequently phenomenon associated with convection like sedimentation and macro-segregation on structure of castings. ESA's next sounding rocket mission, MAXUS-9, is set to be launch in 2016 from the Esrange Space Centre outside of Kiruna, Northern Sweden. It will be carrying furnace module for CET experiments of peritectic TiAl alloys, as seen in Fig. 3.1.

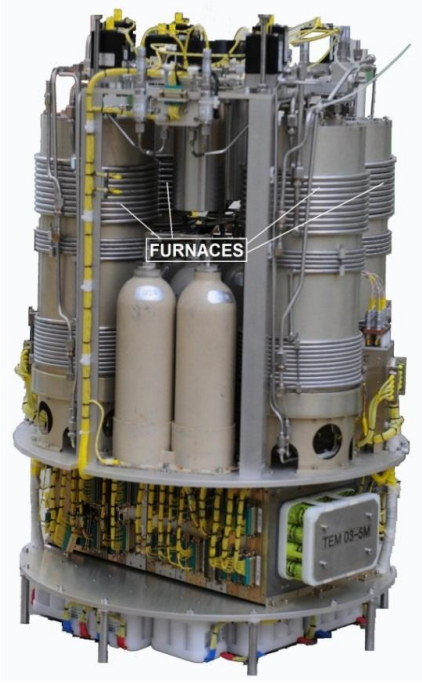

Figure 3.1. Designed furnace module for sounding rocket mission MAXUS.

Figure 3.2. Fuselage of sounding rocket MAXUS for experiment modules.

The MAXUS sounding rocket programme is funded by ESA through the European Programme for Life and Physical Science in Space (ELIPS) with the sounding rocket and launch services provided to ESA by an industrial joint venture between EADS Astrium and the Swedish Space Corporation. Launch to landing of the single stage MAXUS sounding rocket will take only about 26 minutes. The 17 m long rocket includes a fuselage (Fig. 3.2) which will contain the experiment modules to be launched (payloads). The MAXUS solid rocket booster will finish burning after a total of around one minute after launch, followed a few seconds later by jettison of the rocket's nose cone. About 90 seconds after lift off the main engine stage (Fig. 3.3) separates from the payload section. The Rate Control System with its nitrogen thrusters will be activated to stabilise the payload and provide for optimal weightless conditions. After a few seconds, with deactivation of the Rate Control System, the research payloads will experience weightlessness on a steep unpowered parabolic trajectory.

Figure 3.3. Nine meter long Castor IVB rocket motor for MAXUS 9 filled with 10 tonnes of solid propellant.

The payloads of the rocket will achieve an apogee of around 700 km before the descent back into earth's atmosphere begins (Figs. 3.4a and 3.4b). This campaign, using a MAXUS sounding rocket, will provide 12.5 minutes of stable weightless conditions. The planned microgravity experiments with the selected peritectic alloys will be the foundation for advancement in production of new lightweight aircraft engine turbines as well as answering two fundamental research questions in materials science: (i) how does gravity affect the alloy's

behaviour, as it transforms from liquid to solid and (ii) how does gravity shape the structure that forms during solidification process. By varying different process parameters such as temperature gradients, it becomes possible to study other phenomena such as structural transition, segregation of alloying elements and effects of minor alloying elements on the grain refinement. Performing identical ground based and hyper-gravity experiments and comparing results it is possible to examine the effects of gravity induced fluid flow during solidification, which will help to refine theoretical models of solidification.

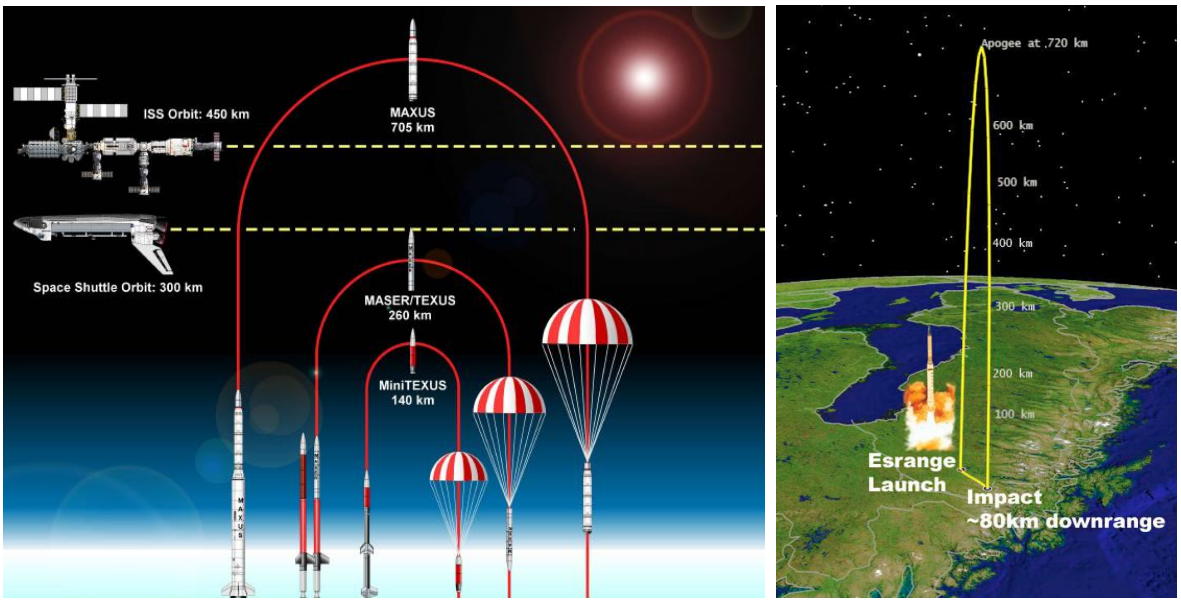

(a) (b)

Figure 3.4. (a) ESA sounding rockets: MiniTexus - apogee of 140 km, microgravity time of 3-4 min.; Texus/Maser - apogee of 260 km, microgravity time of 6 min.; Maxus - apogee of 705 km, microgravity time of 12.5 min. (b) Graphics providing an idea of a MAXUS launch profile.

For ground based experiments, Bridgman type furnace has been redesigned to achieve CET in selected TiAl alloys using power down technique, as seen in Fig. 3.5. The new design of the furnace allows performing CET experiments on cylindrical samples under controlled solidification conditions. The CET experiments are conducted in dense high purity Y_2O_3 crucibles under an argon atmosphere. The power down technique consists of: (i) heating of the sample to a temperature at a constant heating rate, (ii) stabilization at the temperature, (iii) partial displacement of the sample from the hot zone of the furnace into the

crystallizer, (iv) temperature decrease at constant cooling rates and (v) furnace cooling of the sample to room temperature.

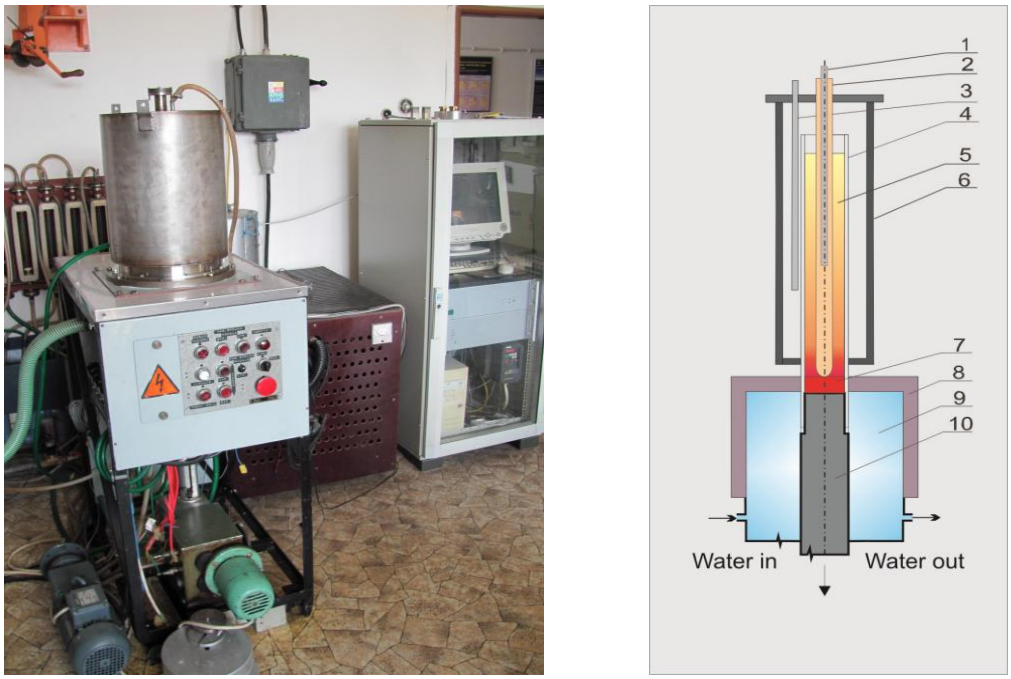

Figure 3.5. Redesigned Bridgman type apparatus for ground based solidification and CET experiments of TiAl alloys: 1 - measuring thermocouple, 2 - ceramic tube, 3 - control thermocouple, 4 - Y_2O_3 crucible, 5 - solidifying sample, 6 - resistance heater, 7 - solid part of the sample, 8 - crystallizer, 9 - water bath, 10 - withdrawal rod.

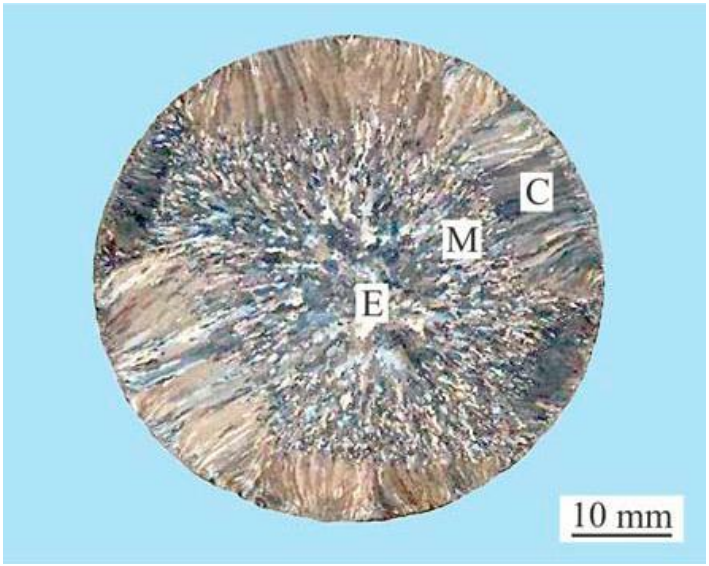

Figure 3.6. Typical macrostructure on transversal section of the as-cast ingot.

Fig. 3.6 shows the typical macrostructure observed on transversal sections of the as-cast ingot from Ti-44.5Al-5Nb-0.2C-0.2B (at %) alloy. Three zones with different type of microstructure designated as C, M and E can be well distinguished. Thin chill zone composed of fine equiaxed grains in the vicinity of the surface of the ingot is followed by columnar grain zone C. The mixed zone (M) is composed of columnar and equiaxed grains. The CET is complete in the central equiaxed zone (E) of the ingot.

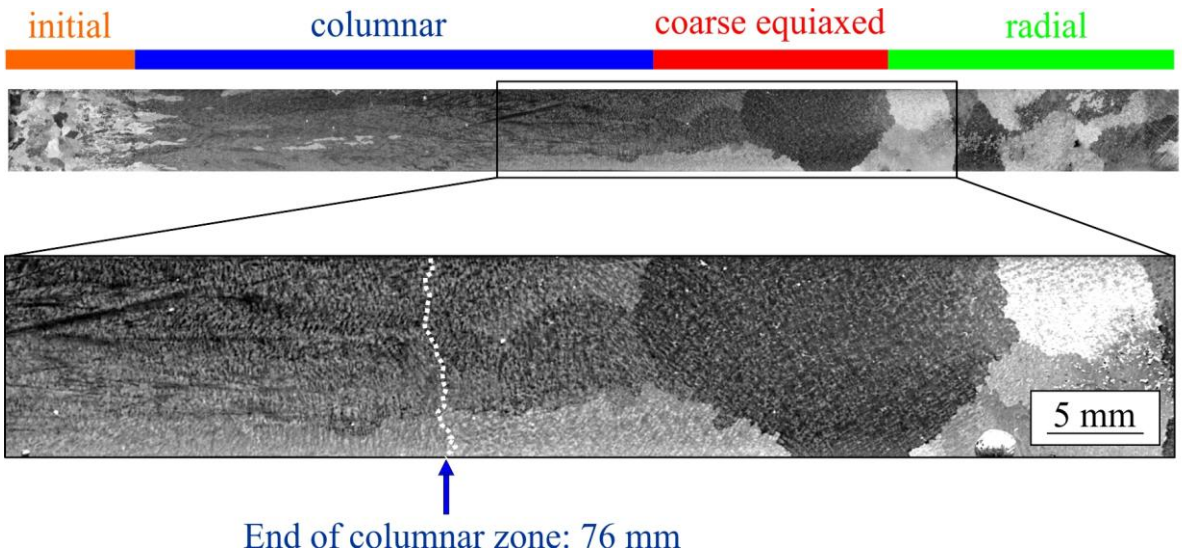

Figure 3.7. Macrostructure of longitudinal section of CET sample prepared power-down technique at a constant cooling rate.

Fig. 3.7 shows the typical macrostructure of the samples prepared by power down technique. The macrostructure consists of four different zones designated as initial, columnar, coarse equiaxed and radial. The initial zone represents non-melted part of the sample composed of equiaxed grains. The columnar zone is composed of columnar grains which were formed during partial displacement of the sample from the hot zone of the furnace into the crystallizer followed by the columnar grains formed during power-down cycle at a constant cooling rate. The coarse equiaxed zone is composed of large equiaxed grains with various crystallographic orientations formed in the liquid during solidification. The radial zone is composed of the grains nucleating at the crucible wall and growing in a radial direction towards the centre of the sample during cooling.

In the studied peritectic TiAl alloys, the α phase is formed through peritectic reaction/transformation of the type: liquid + bcc β(Ti) → hcp α(Ti) during cooling. This means that the grain morphology revealed by the etching is not the one of the β primary solidification phase, but one of the α phase formed by solid state transformation and peritectic reaction/transformation. Hence, such grain structure has no direct relationship to the primary dendrite grain structure and cannot be related to the mechanisms and position of CET in the samples. Therefore, it was necessary to reveal the original primary β phase grain structure to assess correctly the CET phenomena in peritectic TiAl alloys.

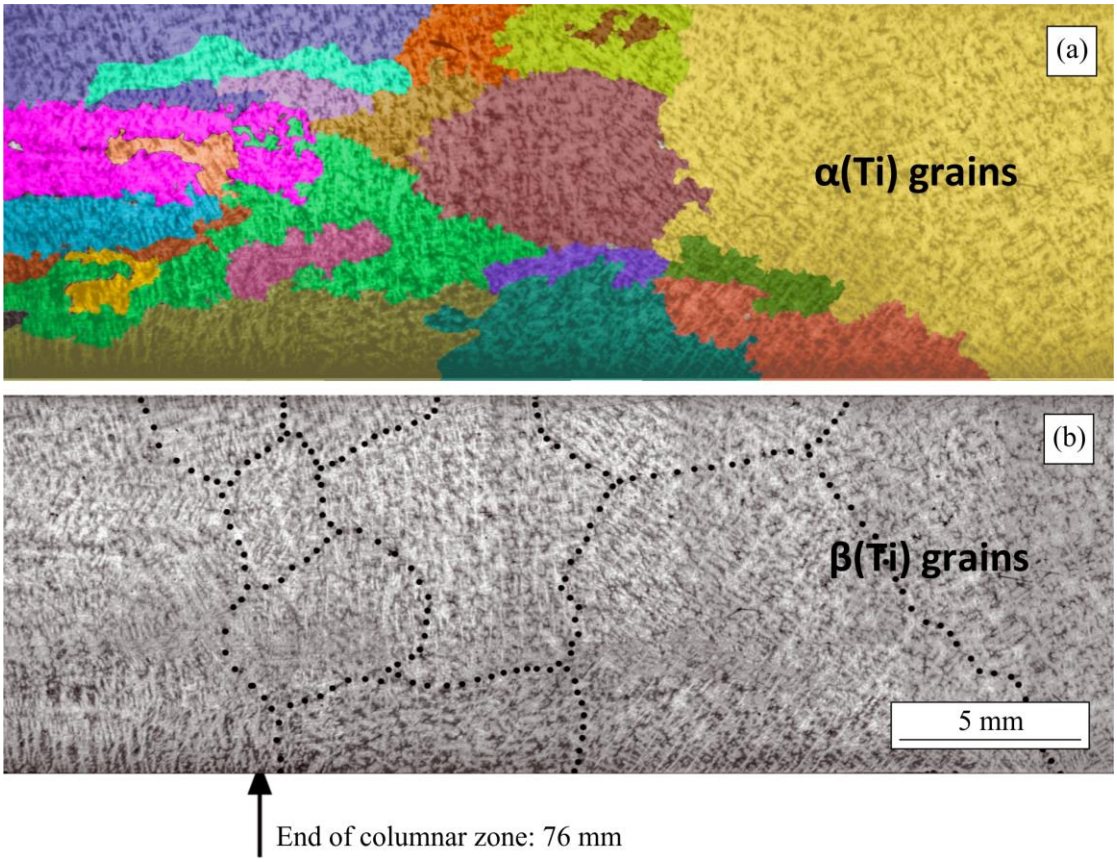

Figure 3.8. Grain structure of a CET sample prepared by power-down technique: (a) columnar and equiaxed α(Ti) grains in the vicinity of CET, (b) columnar and equiaxed β(Ti) grains in the vicinity of the CET.

The analysis of the α phase grain structure formed by solid phase transformation of the primary β phase and peritectic reaction/transformation indicates an apparent mixed zone of columnar and equiaxed grains between the columnar and equiaxed zones of the samples, as seen in Fig. 3.8. Under grazing light, the resulting map shows the α(Ti) grains, i.e. the grains formed through peritectic

reaction/transformation in the deep mushy zone of the sample, see Fig. 3.8a. Under flat light, the dendrite structure of the primary β(Ti) phase grains can be clearly seen, as shown in Fig. 3.8b. It is clear that the α grain structure of the sample differs significantly from that of the primary β phase grains. The studied alloy shows sharp CET when the β primary grain structure is correctly analyzed using.

Fig. 3.9 shows the typical macrostructure of the samples prepared by power down technique in Bridgman type apparatus used for measurements of microsegregation behaviour of main alloying elements. The macrostructure is divided to five zones designated as U, C1, C2, M and E. The zone designated as U represents the non-melted part of the sample composed of equiaxed grains. The zones C1 and C2 are composed of columnar grains which were formed at different solidification parameters. The mixed zone M represents microstructure composed of columnar and equiaxed grains. In this zone, the equiaxed lamellar grains are distributed preferentially between the columnar grains. The equiaxed zone E contains relatively large equiaxed grains with an average diameter of 4.0 mm. Fig. 3.10 shows the variations of segregation deviation parameters for Al, Ti and Nb with the analysed zones C1,C2, M and E in CET sample prepared by power down technique. It should be noted that the calculated segregation deviation parameter is the highest one for Nb in the zone C1 and decrease towards the zone E. The segregation deviation parameters for Al and Ti are significantly lower than that for Nb and decrease from the zone C1 towards the zone E. Fig. 3.11 shows variations of the segregation deviation parameters for Al, Ti and Nb with the analysed zones C, M and E for the BP and UP of the ingot (see Fig. 3.6). The segregation deviation parameter is the highest one for

Figure 3.9. Typical macrostructure of longitudinal section of sample prepared by power down technique in Bridgman type apparatus.

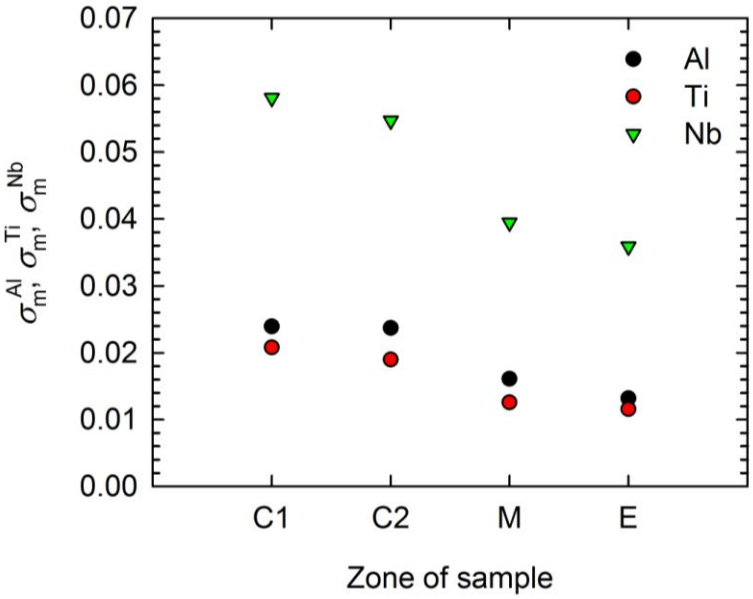

Figure 3.10. Variation of the segregation deviation parameter for Al, Ti and Nb with the columnar (C1 and C2), mixed (M) and equiaxed (E) zone in the sample prepared by power down technique.

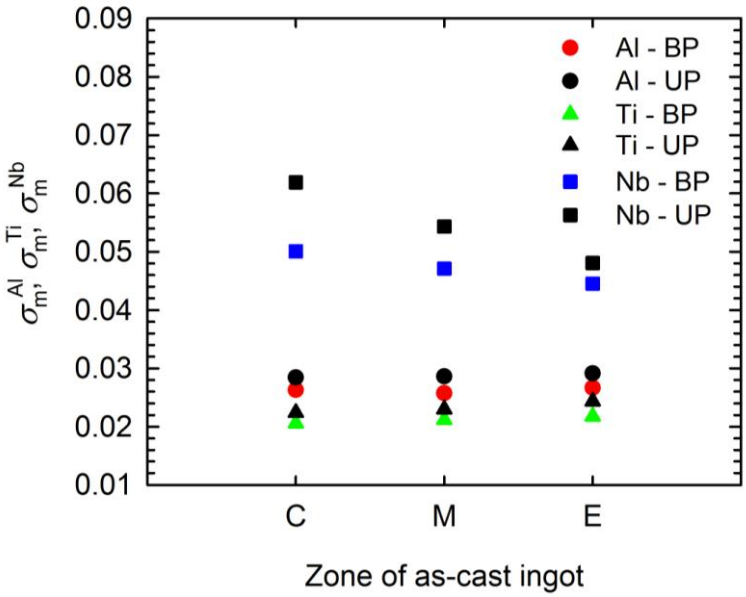

Figure 3.11. Variation of the segregation deviation parameters for Al, Ti and Nb with the columnar (C), mixed (M) and equiaxed (E) zone in the as-cast ingot. BP – bottom part of the ingot; UP – upper part of the ingot.

Nb in the zone C and decreases towards the equiaxed zone E in both the parts of the ingot. The segregation deviation parameters for Al and Ti are significantly lower than that of Ti and their variation with the analysed microstructural zones is negligible for both the parts of the ingot. It is clear from Figs. 3.10 and 3.11

that while the calculated segregation deviation parameters for Al and Ti decrease from columnar to equiaxed zone in the samples prepared by power down technique, these parameters show no evolution with the local microstructure in the as-cast ingot.

References:

3. LAPIN, J. – GABALCOVÁ, Z. – HECHT, U. – MOONEY, R.P. – MCFADDEN, S.: Columnar to Equiaxed Transition in Peritectic TiAl Based Alloy Studied by a Power-Down Technique. Accepted for publication in Materials Science Forum.
4. LAPIN, J. – KLIMOVÁ, A. – GABALCOVÁ, Z.: Effect of columnar to equiaxed transition on microsegregation behaviour of main alloying elements in peritectic TiAl-based alloy. Kovove Mater., 51 (2013) pp. 147-154.
5. KLIMOVÁ, A. – LAPIN, J. – PELACHOVÁ, T. – NOSKO, M.: Effect of solidification parameters on microsegregation behaviour of main alloying elements in a peritectic TiAl based alloy. Kovove Mater., 51 (2013) pp. 89-99.
6. KLIMOVÁ, A.: Columnar to equiaxed transition in the intermetallic titanium alloys (PhD Thesis). Materiálovotechnologická fakulta, 2013. Materiálovotechnologická fakulta STU v Trnave.
7. MOONEY, R. P. – MCFADDEN, S. – GABALCOVÁ, Z. – LAPIN, J.: An experimental-numerical method for estimating heat transfer in a Bridgman furnace. Applied Thermal Engineering, 67 (2014) pp. 61-71.

4. REMOTE SENSING

I. Barka, T. Bucha, J. Feranec, M. Kopecká, J. Nováček, R. Pazúr, I. Sačkov, J. Sládek, M. Sviček, J. Vladovič

Selected activities of five institutions are included to this report:

Institute of Geography, Slovak Academy of Sciences (IG SAS) in Bratislava participated in the second part of the **Urban Atlas** project (2013-2015, Copernicus – GMES – Global Monitoring for Environment and Security) – with the aim to produce the series of land cover/use maps of large urban zones (LUZs, 13 urban classes, 10 other classes) spread over the European countries by using satellite data (total of 700 LUZs). The task of IG SAS together with the expert team from IGN France International is the external quality control which consists of a visual interpretation of points distributed regarding a specific random oriented sampling methods (Fig. 4.1). The interpretation is based on SPOT5 satellite images of the reference year 2012 +/- 1 year which are made available by the European Commission through ESA.

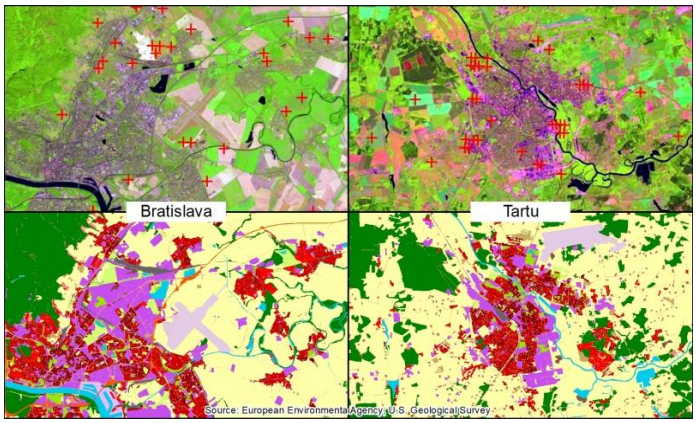

Figure 4.1 Large urban zones of Bratislava and Tartu.
Red crosses identify the control points which are visually interpreted by experts.

IG SAS in cooperation with the National Institute of Geophysics, Geodesy and Geography of the Bulgarian Academy of Sciences **documented urbanization trends in selected regional cities in Slovakia and Bulgaria using VHR satellite data.** Satellite images collected by IKONOS in 2002 (spatial resolution PAN 1 m and MS 4 m) and WorldView2 in 2011 (PAN 0,5 m

and MS 2 m) were used as information source about land cover of the city of Trnava (Fig. 4.2). The detailed land cover maps were the results of local mapping applying the extended CORINE land cover nomenclature for artificial surfaces with the minimum mapped area of 0,25 ha and the minimum width of 10 m. In order to assess the urbanizing trends the following processes were defined: urban extension, urban infill and other changes of urbanized landscape. The results show the global progression of the built-up areas both in Slovakia and Bulgaria.

Figure 4.2 Classification of urban growth in Trnava in the period 2002 2011 based on VHR satellite data.

IG SAS has started to use **the Micro UAVs – new technology of spatial data acquisition.** Micro UAVs (Unmanned Aerial Vehicle) are small remote controlled aerial vehicles up to 5 kg of total weight. Nowadays there are different types of these vehicles – ranging from wing to (multi)rotor based. Since 2013 Institute of Geography Slovak Academy of Sciences has been trying to implement this technology into large- or middle- scale landscape studies – mainly in fluvial geomorphology. Multirotor technology with six propellers (hexakopter) stabilized with accelerometers, gyroscopes and GPS units is used (Fig. 4.3). Whole device is about 80 cm wide and its payload is about 1500 g. Total weight of this device is about 4.5 kg. There is the possibility of using different DSLR cameras, small spectral cameras, small LIDARs or camcorders as data collectors. With these sensors data for creating orthogonal or tilted aerial images, orthophotos, DEMs, point clouds, 3D models of different types of objects or volumetric changes calculation can be collected. Flight time is about 10 – 15 minutes (depending on the payload). Maximal speed is about 60 km/h. Maximum theoretical operational radius is about 1.5 km (transmitter range), but

practically it is about 300 m depending on the pilot skills. Flight altitude reaches several hundred meters, but for aviation safety flight altitude is restricted under certain condition to 120 – 150 m. High resolution images were obtained with Nikon D90 DSLR + Nikon 35mm F1.8 AF-S DX lens.

In the past processing of images was not so easy, because of missing internal and external parameters of images. Nowadays there are numerous open sources, or commercial software which can compute these parameters directly from exif file and from images specially used for lens calibration. Specialized software is able to create orhophoto mosaics, DEMs, 3D models or point clouds.

In 2013, several studies aimed at identifying the potential of this method for geography and landscape studies were carried out. We established a monitoring site near Stropkov where we are going to study evolution of avulsion channel of Ondava river created during three flood events in 2010. We created orthophoto mosaic of this area and in the future we want to continue with aerial mapping of this site after every flood event (Fig. 4.4).

Next study was aimed at point cloud creation of a part of river dyke near Devínska Nová Ves to evaluate density of point cloud obtained from UAV by close range photogrammetry techniques and its quality compared to terrestrial LIDAR data (Fig. 4.5).

Figure 4.3 An example of multirotor UAV. Six-rotor remotely controlled flying platform with Nikon D90 DSLR + Nikon 35mm F1,8G AF-S DX lens.

Realistic 3D photomodeling using UAV and close range photogrammetry was realized in Bernolákovo at the archaeological site of Čeklís (Fig. 4.6).

In next research we have an ambition to use this technology for monitoring of river bank erosion, river bed changes, slope deformations, landscape and landform mapping and so on.

Figure 4.4 A part of ortophoto mosaic of avulsion channel of Ondava river near Stropkov, processed in Airphoto SE. Captured area is about 3.5 ha. Total number of orthorectified pictures – 67 taken from altitude of 70 m. Pixel resolution is 2cm and positional precision of area is subdecimetre.

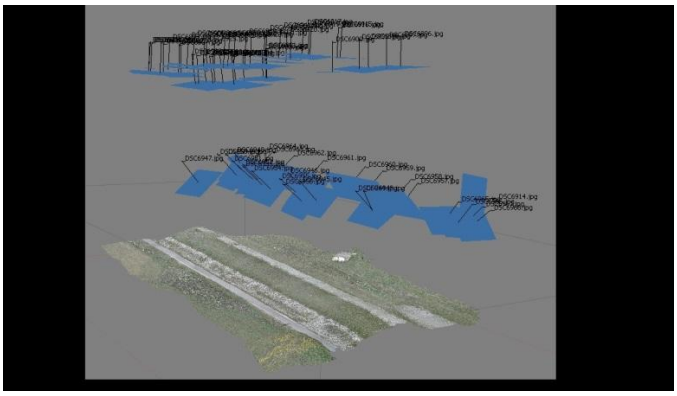

Figure 4.5 Colorized point cloud of part of river dyke near Devínska Nová Ves with camera positions (blue rectangles). Point cloud is processed from 72 orthogonal and tilted pictures taken from altitude 35 and 60 m. Point cloud was processed in Agisoft PhotoScan with subdecimetre precision of whole block.

Figure 4.6 Photorealistic model of archaeological site of Čeklís. Model was created from aerial images and ground images in Agisoft PhotoScan.

Activities of the **Slovak Environmental Agency (SEA)** in Banská Bystrica were concentrated on the solution of **Copernicus and GIO land 2011-2013** project.

Programme Copernicus (until the end of 2012 the name of the programme was G.M.E.S) is European programme for Earth Observation. In the years 2012 and 2013 programme Copernicus was in its Initiation phase. The work on the programme was concentrated on cooperation with GMES Committee and GMES User forum and commenting on the EU level technical and legislative documents regarding the programme. At the national level the aim was on establishing national framework for the cooperation of governmental and public organizations regarding the programme. At December 2013 the government of the Slovak Republic ratify government Regulation with the goal to establish National working group for Copernicus latest at June 2014. The working group will coordinate actions of government and public organizations a disseminate information regarding programme Copernicus to public.

Slovak Environmental Agency (SEA) joined the activities in project "Initial Operations (GIO) Land Monitoring 2011 – 2013 in the framework of regulation (EU) No 911/2010". Project is coordinated by European Environmental Agency (EEA). The contract between SEA and EEA was signed in October 2012.

This project consists of four different tasks:

- Verification of the 5 High Resolution layers (HRL's)
- Enhancement of the 5 HRL's
- CORINE land cover changes 2006-2012 and CORINE land cover 2012
- Dissemination activities (INSPIRE map services)

SEA is project partner for EEA in all of these tasks. On national level, SEA has subcontract with experts from Forest Research Institute (NFC) and Soil Science and Conservation Research Institute (SSCRI).

One of the new tasks in this contract is verification and enhancement (HRL's). HRL`s are produced by services provider (different contract between EEA and Services provider – for LOT 3 – GAF AG) for five land cover type imperviousness, forests (tree cover density and forest type), grass-lands, wetlands and permanent water bodies. In the period 2012-2013, Slovak environmental agency verified the HRL Imperviousness (63% of the territory,

see Fig. 4.7) and Forest Research Institute verified the HRL Forests – Forest type and Forest density (see Fig. 4.8). RapidEye and IRS-P6 LISS-III were source for generate HRL. Two different methods are used for verification. First method is "Look & feel" which is obligatory and second method is the method of the quantitative verification].

Figure 4.7 Example of the HRL Imperviousness layer.

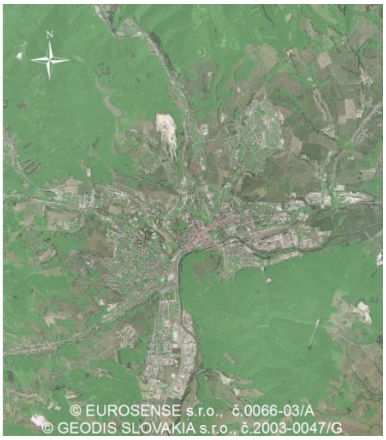

Figure 4.8 Example of the HRL Forests layer.

Next task which started in the period 2012-2013 was mapping CORINE land cover changes 2006-2012 (CLC-Change2006-2012) and CORINE land cover 2012 (CLC2012). Satellite images (Fig. 4.9) for interpretation were made available and downloaded from The European Space Agency (ESA) data warehouse and after them prepared for interpretation - (clouds masking and generating images in false colour). Resolution for satellite images for IRS-P6

LISS III and RapidEye is 20 m/pix (National level). Computer assisted photointerpretation of the changes (CLC-Change$_{2006-2012}$) is in process. Actual is processed 75% of the territory.

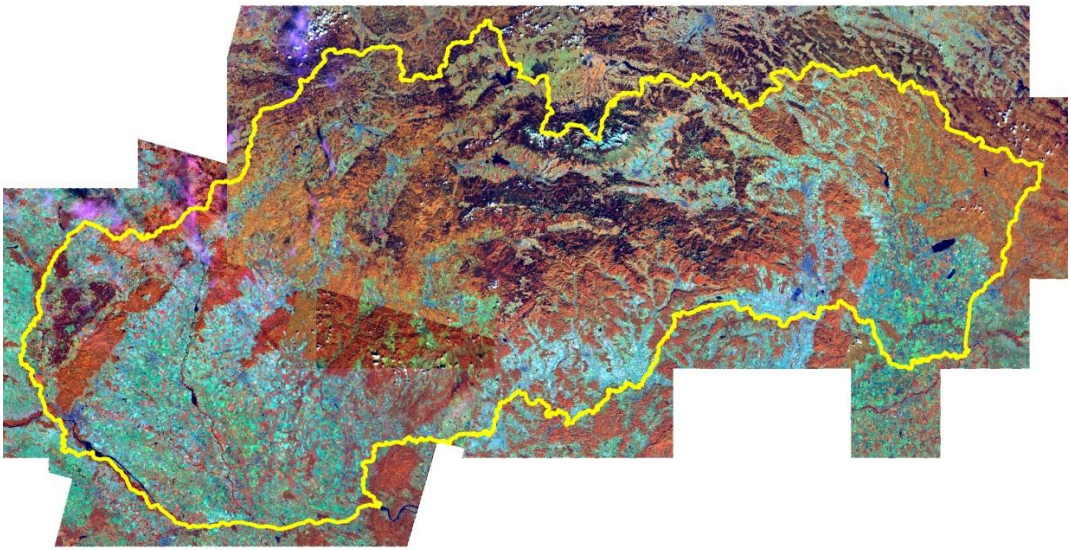

Figure 4.9 IMA2012 coverage 1 – mosaic of the IRS-P6 LISS III in false colour.

Remote sensing oriented projects and activities of the **National Agricultural and Food Centre – Soil Science and Conservation Research Institute** in Bratislava:

Remote sensing control of area-based subsidies in agriculture (2012-2013)

The subsidies play a key role in agriculture sector and contribute to the prosperity of agricultural subjects. The subsidies to agriculture sector represent major part of European budget and that's why there is taken an emphasis to the control.

On the following figure the distribution of the control sites can be seen. The Slovak Administration has chosen six control sites in 2012 defined by 530.6 km^2 in DELU, 225 km^2 in LENZ, 600 km^2 in LURS, 225 km^2 in NMTN, 600 km^2 in SABI and 480 km^2 in SEMY (Fig. 4.10). For the 2013 campaign the Slovak Administration decided to have also six control sites defined by 478.1 km^2 in BAPA, 150 km^2 in KODV, 150 km^2 in KOJE, 651.8 km^2 in MITR, 477.6 km^2 in

NAME and 434 km^2 in NOLE (Fig. 4.10). They cover approximately 5 % of the applications in 2012 and 7 % of the applications in 2013.

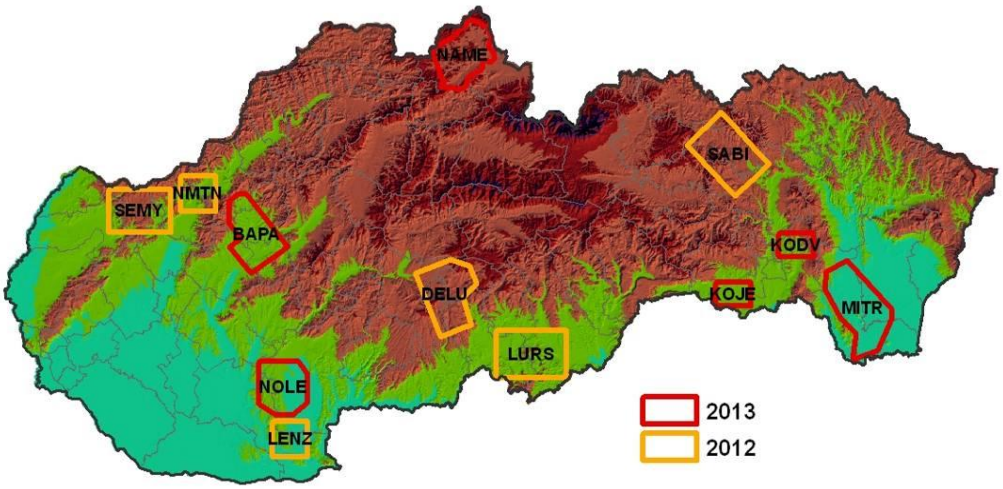

Figure 4.10 Localization of the controlled sites in campaigns 2012 and 2013.

In control procedure a set of high resolution (HR) multispectral images as SPOT4, SPOT5 and THEOS 1A were used for precise identification of grown crop (Fig. 4.11). Two HR acquisition windows were used: HR-1 and HR+1.To control the cultivated area and the usage Very High Resolution (VHR) images from IKONOS2, GeoEye1 and EROS-B and FORMOSAT2 as back-up images were used per each site (Fig. 4.12). Features which have to be excluded from the parcels like field path, straw stacks, midden, etc. are well recognisable on these images.

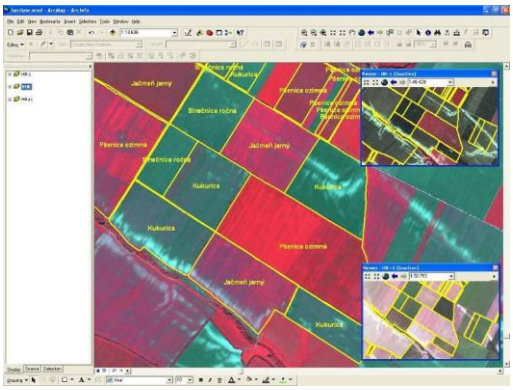

Figure 4.11 Example of land use check on HR images from different acquisition windows.

The CAPI (Computer Assisted Personal Interviewing) has been adjusted to the annual conditions of the regulations of subsidy schemes. Approximately

58 000 graphical annexes were printed and delivered to the farmers where they indicated the agricultural parcels they cultivate.

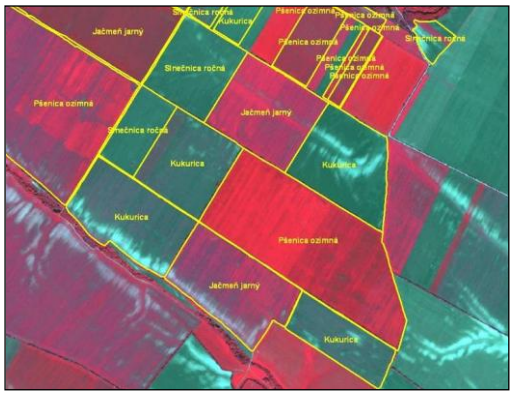

Figure 4.12 Example of boundary check on GeoEye1 image (VHR).

In 2012 campaign the total number of applicants was 16 470, the number of dossiers controlled with remote sensing was 873. The total area controlled was 103 151.48 hectares, with 7 318 reference parcels. There were 10 646 agricultural parcels to control (in 3 schemes), on average *12* parcels/farmer and 89, 46 hectare/dossier. According to the final diagnosis, which summarizes the diagnoses of the conformity and completeness tests at dossier level, 271 (31.04 %) dossiers were accepted for Single area payment scheme, 232 (26.58%) for Complementary National Direct Payment scheme and one dossier for Special Protection Areas for birds.

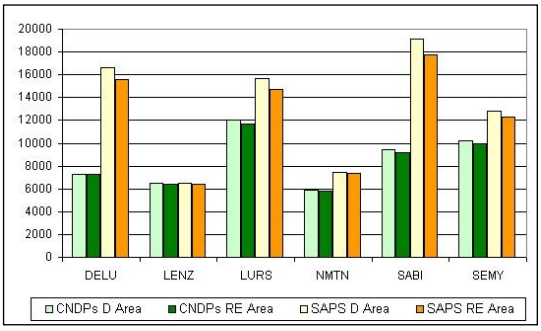

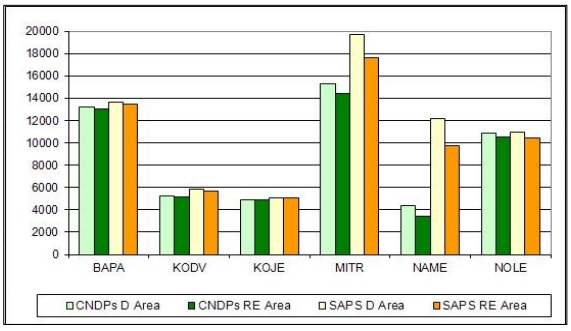

Figure 4.13 Declared and retained area (ha) for schemes CNDPs and SAPS per site.

In 2013 campaign the total number of applicants was 17 058, the number of dossiers controlled with remote sensing was 1192 (6.99 % of all dossiers). The total area controlled was 99 540.78 hectares, with 4 324 reference parcels. There

were 16 528 agricultural parcels to control (in 3 schemes), on average *14* parcels/farmer and 56.54 hectare/dossier. According to the final diagnosis, which summarizes the diagnoses of the conformity and completeness tests at dossier level, 560 (46.97 %) dossiers were accepted for Single Area Payment Scheme (SAPS), 518 (43.45%) for Complementary National Direct Payment (CNDP) scheme and one dossier for Special Protection Areas for birds (Fig. 4.13).

Remote sensing within crop yield and crop production forecasting (2012-2013)

Monitoring of Crop Conditions and Crop Monitoring

Regional monitoring of natural crop conditions aims to study the influence of weather (coupled with soil) on crop growth and crop development during current vegetation season.

4.14a 4.14b

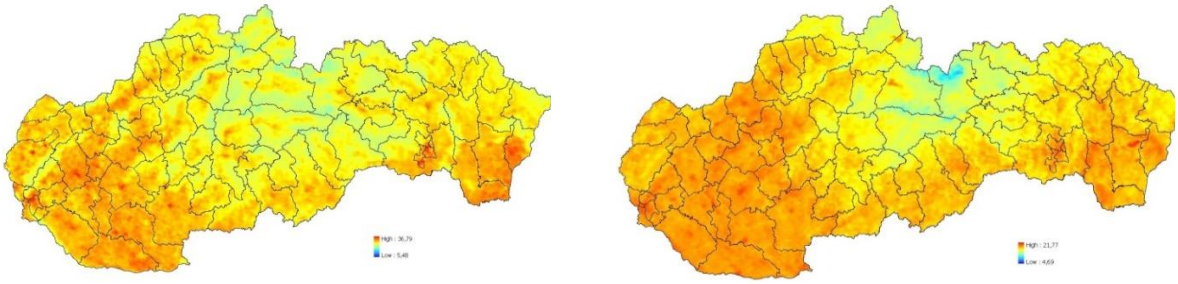

Figure 4.14 Day (4.14a) and night land surface temperature average (4.14b) in the third decade of July 2013.

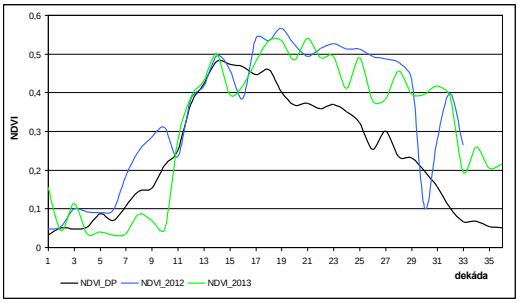

Figure 4.15 Comparison of NDVI development in 2012, 2013 and NDVI long term average.

Day and night land surface temperature and also NDVI (Normalized Difference Vegetation Index, see Fig. 4.15) are derived from NOAA's AVHRR sensor (Fig. 4.14).

Crop yield forecasting

The aim of the crop yield and crop production forecasting is to provide the most likely, scientific, as precise as possible and independent forecast for main agricultural crop yields for Ministry of Agriculture and Rural Development of the Slovak Republic and for the public.

National Crop Yield and Crop Production Forecasting System has been created on SSCRI and is based on three different principles which are applied to specify vegetation indexes as biomass development stage and biomass development:

- Remote Sensing method – method of interpretation of vegetation indicators (as NDVI or DMP – Dry matter development) from satellite images (mainly from low resolution satellite sensors as NOAA AVHRR and SPOT Vegetation satellite system);
- Bio-physical modeling (WOFOST model) and simulation of vegetation indexes (mainly TWSO – Total Dry Weight of Storage Organs and TAGP – Total Above Ground Production). In WOFOST, weather and phenological data, soil hydro-physical data and crop physiological data are utilized as model key inputs;
- Integrated assessment method, which means the implementation of specific meteorological and vegetation indicators in the statistical analysis, assesses the impact of weather on the projected harvest. Integrated estimate summarizes a wider range of disparate indicators and indices that are currently for the purposes of forecasting yields and consequently the production of crops used.

The crop yield and crop production forecasting is carried out for main agricultural crops – winter wheat, spring barley, oil seed rape, grain maize, sugar beet, sunflower and potatoes. The forecasts are reported six times per year – in the half of May, June and July for "winter and spring crops" and in the end of July, August and September for "summer crops". The forecast results are

interpreted at national level as well as at NUTS 3 and NUTS4 level. The example of crop yield forecasting in 2013 can be seen in the Fig. 4.16.

- 4.16a

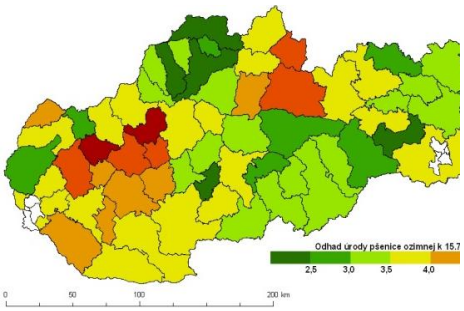

- 4.16b

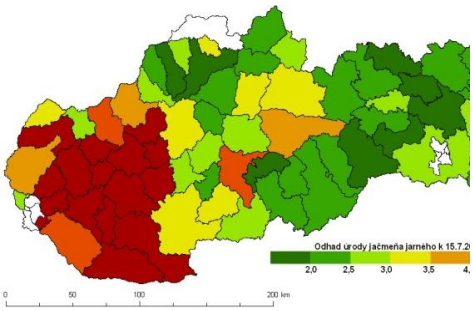

Figure 4.16 Example of crop yield forecasting with remote sensing in first decade of July in 2013: winter wheat (4.16a) and spring barley (4.16b).

Remote sensing research activities of the **National Forest Centre** in Zvolen were solved mainly in the framework of the project *Centrum of excellence for decision support in forest and countryside*[1]. The research was aimed at following topics:

A) Research of the applications of airborne laser scanner technology in the forest management.
B) Satellite-based observation of forest ecosystem's response to global environmental changes.
C) Innovative approaches in mapping and assessing the structure and texture of mountain forest stands in Low Tatras.

A) The research of the applications of airborne laser scanner (ALS) technology in the forest management was aimed at:

Mapping of line objects (forest roads)

The mapping of the forest road network based on the data acquired from ALS on the example of the study area of 150 ha has proven good usability of this technology of remote sensing of the Earth within solving the analysed topic.

[1] This work was supported by Operational Programme Research and Development in framework of the project *Centrum of excellence for decision support in forest and countryside*, ITMS 26220120069.

The terrain models deriving from ALS data enable the exact identification of the majority of forest roads. Only approx. 13% of all permanent roads could not be recorded in the study area from ALS data. At the same time it was possible to record approx. 20% of the roads that were not recorded within the terrain survey of the permanent forest road network (Sačkov et al. 2014).

Example of visibility of forest roads under canopy cover in the terrain model derived from ALS data (2 pt/m^2) is illustrated in Fig. 4.17.

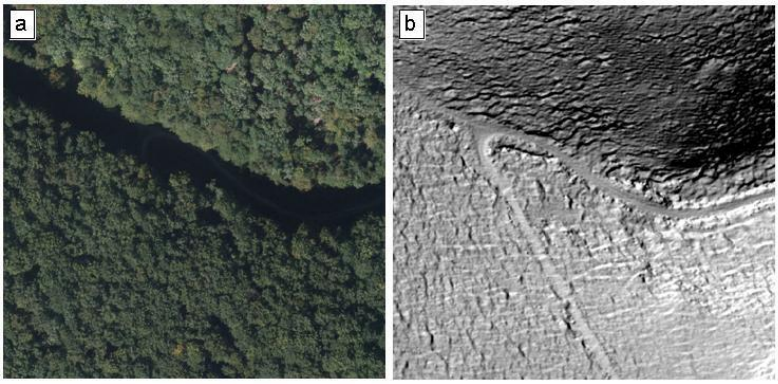

Figure 4.17 Visibility of forest roads under canopy cover: a) Aerial Images; b) DTM from ALS.

Mapping of polygon objects - forest and nonforest area

To assess the possibility of forest boundaries identification based on the ALS data was tested in the study area with an area of 236 ha.

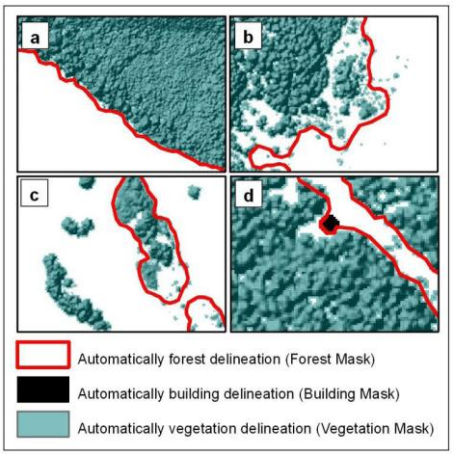

Figure 4.18 Automatic forest delineation based ALS data: a) clear course of the forest boundary; b) ambiguous course of the forest boundary; c) non/forest in vegetation mask; d) use of "Building mask" in forest delineation.

Classification of vegetation and the subsequent application of iterative restrictive criteria of minimum height, width, area, and crown coverage, also considering the spacing of tree crowns and the presence of buildings, ensured an overall accuracy of 93%, K=0.85 (Sačkov & Kardoš 2014).

Example of outputs of the tested approach for automatic forest delineation based on ALS data is illustrated in Fig. 4.18.

B) Satellite-based observation of forest ecosystem's response to global environmental changes – research was aimed at:

Spruce decline in Slovakia

The research focused on assessment of spruce decline using satellite imagery from Landsat in commercially used forest and in small-scaled protected areas as well. The significant worsening of spruce forest condition has been monitored since 2004 due to widespread windbreak followed by outbreak of bark beetle (Fig. 4.19-4.20). Two-phase regression sampling method was applied to assess of spruce forest condition in 2003, 2006, 2007, 2009, 2010, 2011, 2012 and 2013. These classifications were mutually compared. The classifications show that area of damaged increased from 7.8% in 2003 to 21.8% in 2013 on national level. This worsening was even higher in small-scaled protected areas (4^{th} and 5^{th} level of protection) where portion of damaged spruce forest increased from 6.6% to 24.9% (Fig. 4.21). It has raised the questions about suitability of non-intervention regime and about management of protected areas. The level of damage of forest in protected area progressed faster up to 2009 and since that spread more slowly comparing to commercially managed forest. The progress of damage in commercially used spruce forest, where trees affected by bark beetles were continuously removed (active management), shows a more-less linear trend of spruce condition worsening. The spatially distribution of damage area confirmed that spruce is endangered in all area of its occurrence caused by a concurrent impact of biotic, abiotic and anthropogenic injurious agents (Bucha & Barka 2013).

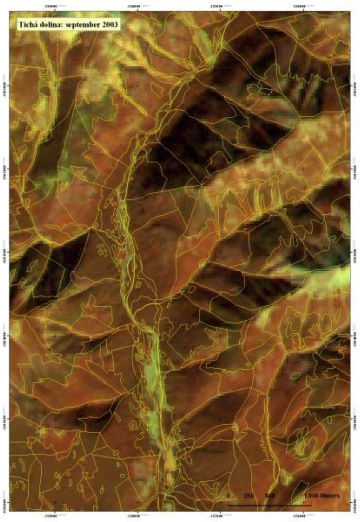

Figure 4.19a Tichá valey in High Tatras National Park. Composition of satellite images Landsat ETM + from 2003 (before windstorm 2004).
Brown colour: undamaged coniferous stands.
Credit: Landsat satellite courtesy of the U. S. Geological Survey (USGA)

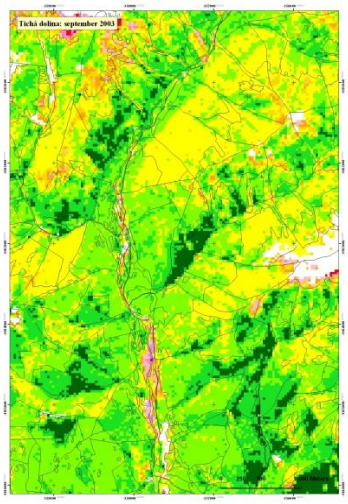

Figure 4.19b Classification of spruce stand's damage in 2003.
size ~ 6 x 4 km.
Black polygons: boundary of forest compartments.
Green colour: healthy stands;
Red colour : Dead stands

Figure 4.20a Tichá valey in 2013.

Credit: Landsat satellite courtesy of the U. S. Geological Survey (USGA)

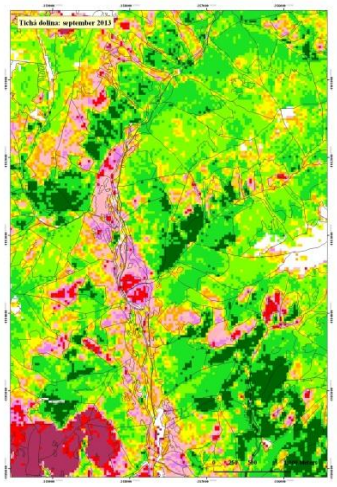

Figure 4.20b Classification of spruce stand's damage in 2013.

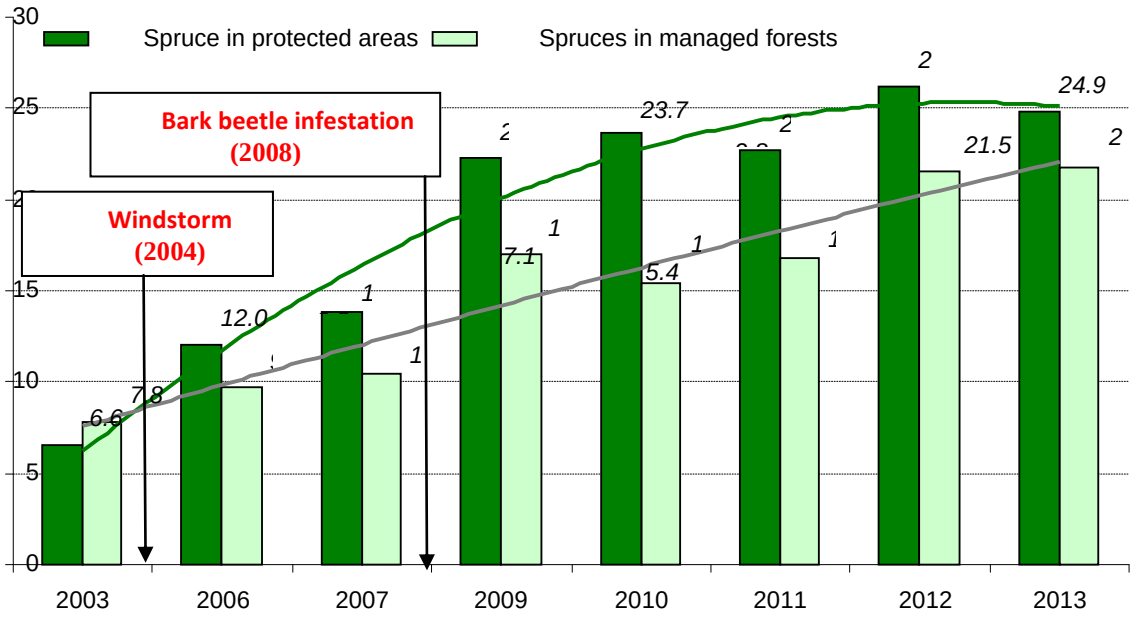

Figure 4.21 Percentage of damaged spruce (defoliation > 40 %) in protected areas and managed forest in 2003–2013.

Development of satellite-based system for a continuous evaluation of forest's response on changed environmental condition

Structure of the information system has been gradually developed and optimized. IS compounds of two subsystems aimed at health (based mainly on Landsat satellite data) and ecological and productive state of forest (based on MODIS medium resolution satellite data). Each subsystem has its own tools for data pre-processing, storage, analyses and publication.

The 1st subsystem is designed to inform forest owners and forest state administration about the actual state of forest stands and its changes. The web service STALES was put into operational mode five years ago (www.nlcsk.org/stales). During last two years the dataset of Landsat images was updated. There were added satellite images from all over Slovakia from 1990, 1996, 1998, 2000, 2003, 2006, 2007 and 2010 to 2013.

The mosaic was created from individual images for each of those years. Forest damage classification layer was derived from the mosaics. Web-map applications are prepared so that boundaries of forest districts are visible at the scale of 1:100 000 and the boundaries of forest compartments at the scale of 1:20 000. Actually STALES consists of 4 map applications:

1) The first map application brings to users mosaics of Landsat satellite imagery and maps of forest health condition from 1990 to the year 2013. The starting point for estimating the damage is to determine defoliation. Forest damage is expressed at a scale from 1 to 11 where: 0 - stands without damage, 10 seriously damaged and dead vegetation, fallen trees and areas after logging. Class 11 in most cases represents a deforested area of after harvesting without vegetation.
2) Dynamic view of historical and recent Landsat satellite images.
3) Dynamic view of map of forest health condition.
   These applications allow users continuously investigate he development of the land cover and forest cover since 1990 until now by simply moving the cursor over a continuous time bar.
4) The latest application allows a comparison of satellite images between selected years using "swipe" tool. The user has to choose the years for the comparison of changes in forest and landscape (Fig. 4.22).

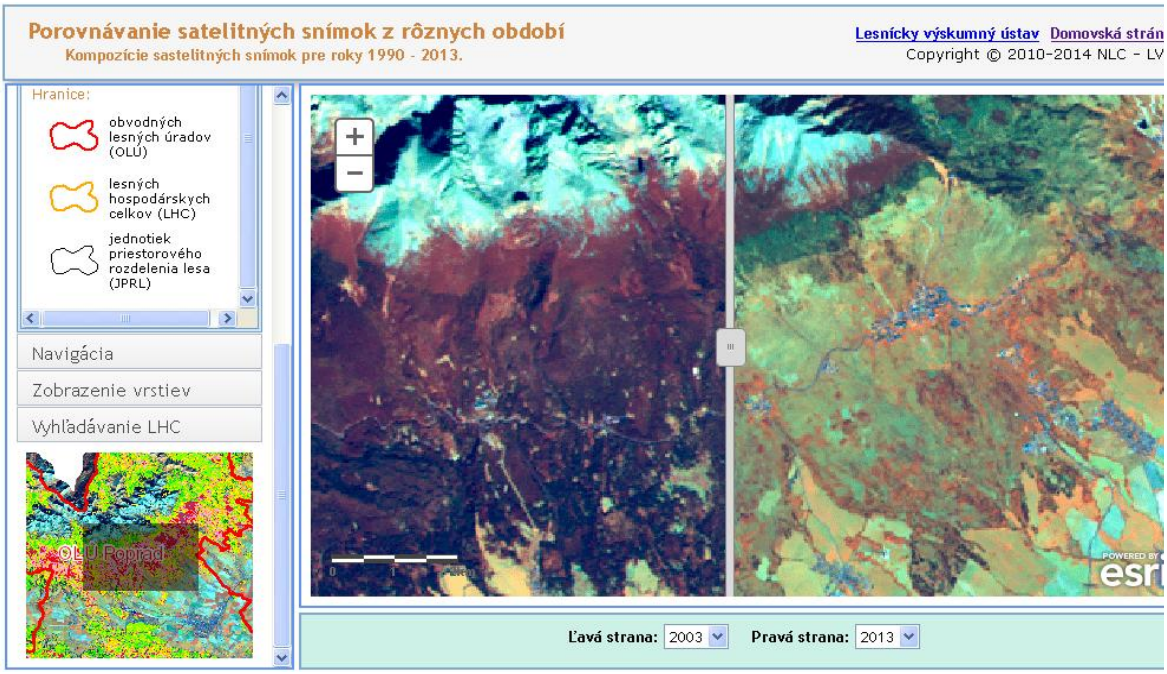

Figure 4.22 Web service http://www.nlcsk.org/stales/ – map application for dynamic comparison of land cover changes on Landsat satellite images between selected years.

Credit: Landsat satellite data courtesy of the U.S. Geological Survey (USGS).

C) Innovative approaches in mapping and assessing the structure and texture of mountain forest stands in Low Tatras.

The work addresses the thematic mapping and assessments of the forest stand structures based on a combination of remote sensing and terrestrial methods using geographic information systems (GIS). Building on our previous research, we proposed the system of thematic mapping of the sets of stand types in the model area Lomnistá Valley in the Low Tatras (1 623 ha), structural types and elements, classification of structure and ecological stability of mountain forests in the localities Konštiaky, Široký úplaz, Martalúzka – Byčiarky in the Low Tatras covering 270 ha. In the locality Medvedia úboč in Lomnistá Valley with the communities of natural forests in the fir-beach altitudinal vegetation zone, the innovative methods of thematic mapping of stand structure types and segments, based on RS, GIS, segmentation methods and mobile technologies, were examined. Stand texture types, elements and segments were identified, localized and partially classified on orthorectified digital multispectral aerial scenes combined with SPOT satellite scene. Historical aerial panchromatic images from the years 1949, 1971 and 1992 were used for interpretation of tendencies and trends in different types of stand textures (Fig. 4.23). Spatial classification was established on the method of image segmentation. In the field, the total 98 segments at higher level covering 63 ha were localized and characterized in detail. A detailed descriptive system of the habitat, conservation, species, spatial and age structure of the segments was used.

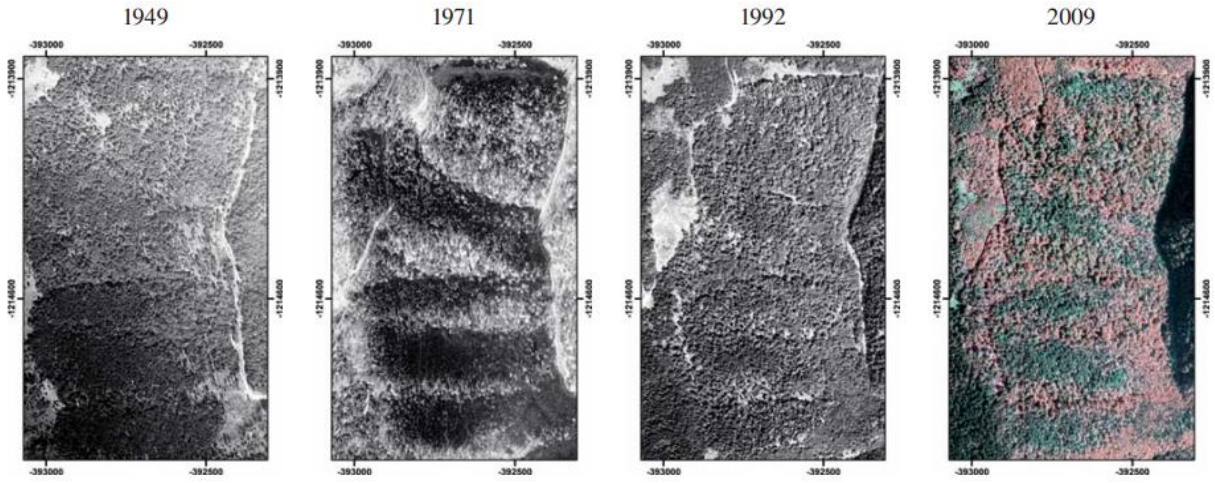

Figure 4.23 Historic aerial photos can be used in interpreting the tendencies and development trends of stand textures in comparison to the current condition of textures in a multispectral aerial image (ML Medvedia úboč).

Research plots, detailed biometrically measured by FieldMap technology, were used as training plots for classification with RS data and as the calibration objects in a spatial description of the segments in the field. The proposed approaches were verified in several model localities with the possibility of generalization for the entire range of forest communities in Slovakia (Vladovič & Bucha 2013).

The new project INMEIN "*Innovative methods for monitoring and inventory of Danube floodplain forests based on 3D technologies of remote sensing*" has started in September 2012. The project is implemented with the financial assistance from the European Union through ERDF under the Cross-Border Cooperation Programme Hungary-Slovakia 2007–2013 (www.husk-cbc.eu). The project develops long-term partnership between National Forest Centre Zvolen and Hungarian Forest Research Institute in Sarvar and University of West Hungary in Sopron. Main subject of the project is to develop innovative methods and support a common approach in forest monitoring in Danube floodplain area influenced by the hydro-power plant at Gabčíkovo according to mutual obligatory cross-border commitments of Hungary and Slovakia.

Aerial based lidar and multispectral photos scanning was successfully done in September 8, 2013. The concept of contactless assessment of tree and stand characteristics i.e. tree diameter, tree height, tree and stand volume were prepared (Fig. 4.24). A field survey was carried out to obtained precise terrestrial data for airborne lidar data validation.

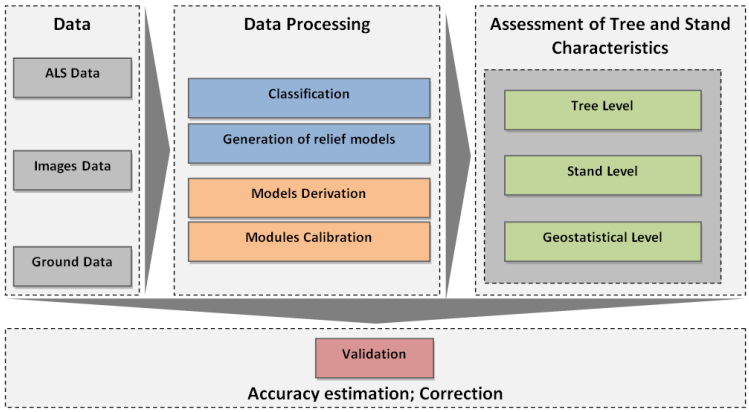

Figure 4.24 The concept of contactless assessment of tree and stand characteristics.

Besides developing algorithms for processing of lidar data an improved procedure of floodplain forest health evaluation was proposed from digital multispectral aerial images (Bucha & Slávik 2013). Firstly, the forest mask was created with overall accuracy 89%, and next, tree health was evaluated using defoliation as health indicator. A forest condition prediction resulted in r-square equal 0.86.

5. SPACE METEOROLOGY.

D. Kotláriková, J. Kaňák, Ľ. Okon, L. Méri, M. Jurašek

5.1 Satellite data applications in INCA-CE Project

INCA-CE Project (ended in September 2013) was devoted to weather nowcasting based on integration of various data sources (Numerical weather prediction model output, station weather data, and radar and satellite observations) into products which are more precise and with higher space and time resolution as input data. Satellite data play important role to control temperature and precipitation fields, both coming from analyses and forecasts. NWCSAF cloud products (Cloud Mask, Cloud Type, Probability of Precipitation, Convective Rainfall Rate and other) are generated for this purposes not only from measured MSG satellite data received regularly at SHMÚ, but also from MSG image data extrapolated in time up to four hours with step of 15 minutes. For extrapolation of satellite imagery algorithm FCI (previously used at SHMÚ for nowcasting) was adopted for 11 MSG SEVIRI spectral channels. Due to extreme volume of extrapolated image data and high time frequency of runs procedure was implemented on supercomputer devoted to NWP model calculations.

Usage of satellite data to control NWP outputs (cloud fields and temperature in 2m) is based on the categorisation of cloudiness from NWCSAF Cloud Mask. The method was developed to differentiate between cloudy and cloud-free areas in NWP cloud cover as a function of satellite cloud types. Because proper temperature forecast depends extremely on proper cloud forecast, cloud index as a result of this categorisation was defined with following values:

1 Cloudy free was forecasted by model and detected by satellite measurement,

2 Cloud was forecasted by model and detected by satellite measurement,

3 Cloud was not forecasted but detected by satellite measurement,

4 Cloud free was not forecasted but detected by satellite measurement.

Radiation conditions differ significantly for cloud indices 3 and 4 and model temperature forecast fails in these areas (see Fig. 5.1, left). To correct failed forecasts of temperature we calculated temperature bias for each cloud index by comparing model output and ground measurements (Fig. 5.1, right). INCA temperature analysis was considered as a ground truth in this comparison. Example of situation with no significant bias distribution is shown in Fig. 5.2, when Gaussian distribution of temperature differences for various cloud indices is not shifted. Another case with very significant bias is shown in Fig. 5.3, where we observed mutual shifts between temperature differences belonging to properly and improperly forecasted cloudy and cloud free areas.

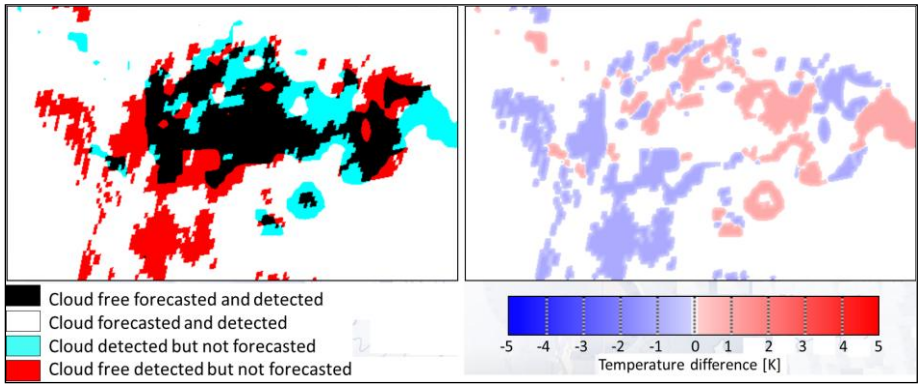

Figure 5.1 Cloud Index derived for INCA SK (Slovak domain) using satellite data (left) and Temperature Biases – correction field derived using Cloud Index and by comparison NWP and ground measurement data. Valid for 22 December 2012, 3:00UTC.

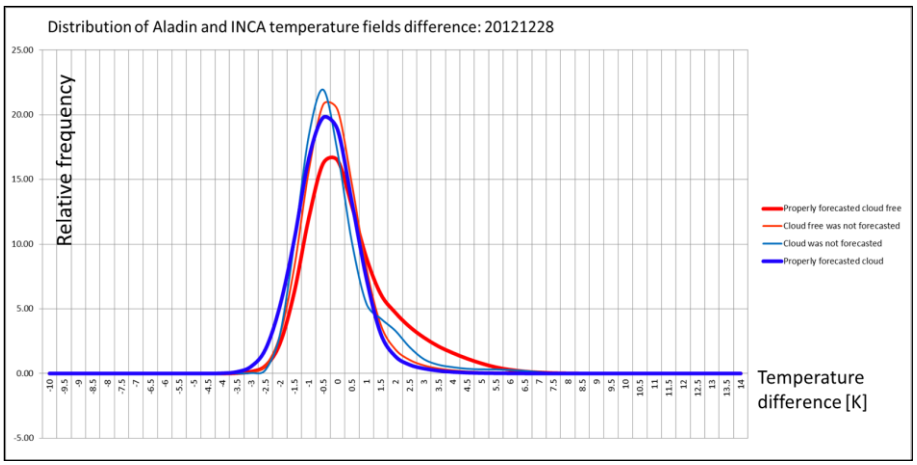

Figure 5.2 Distribution of NWP output and INCA temperature biases for 28 December 2012. For all cloud indexes biases are near zero, correction of temperature is not necessary.

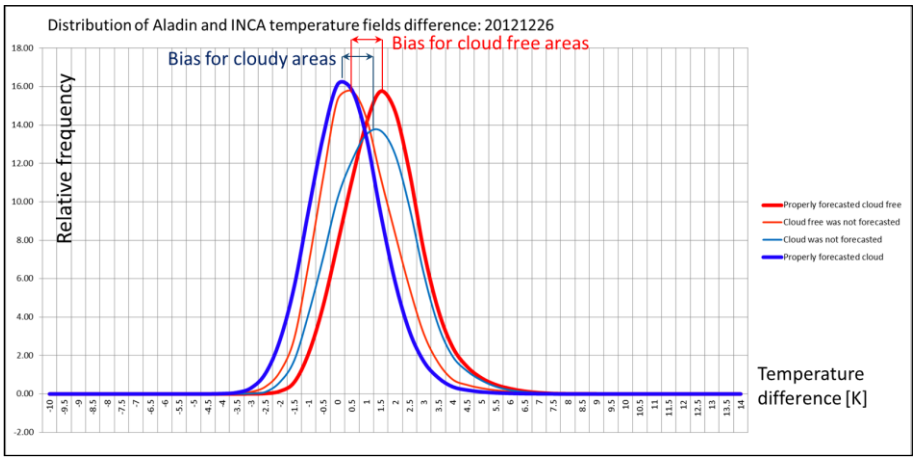

Figure 5.3 Distribution of NWP output and INCA temperature biases for 26 December 2012. Significant bias for cloudy and cloud free areas, correction of temperature is necessary to be applied.

When control of NWP cloud fields is done for time sequence, we can find certain time periods, when no correction of modelled temperature is necessary and also periods, when significant bias for cloudy or for cloud free areas is observed. Example is shown in Fig. 5.4. Temperature biases are not applied directly but through INCA re-analyses of temperature fields. In this way not only current temperature field but also temperature forecasts can be corrected. Impact of corrections was observed up to 12 hours forecasts. Example of uncorrected and corrected temperature field over Slovakia is shown in Fig. 5.5.

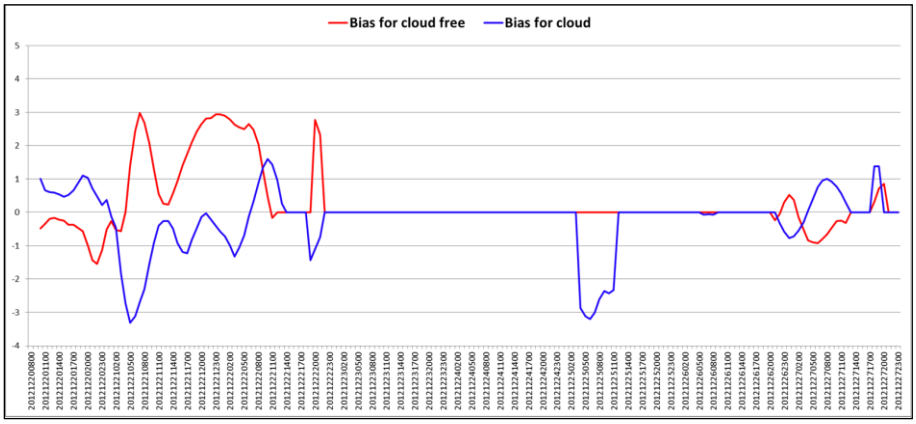

Figure 5.4 Time changes of temperature bias identified for cloud free and cloudy areas using satellite and NWP cloud comparison. Biases are usually complementary, which result from radiation balance between land surface, atmosphere and cloudiness.

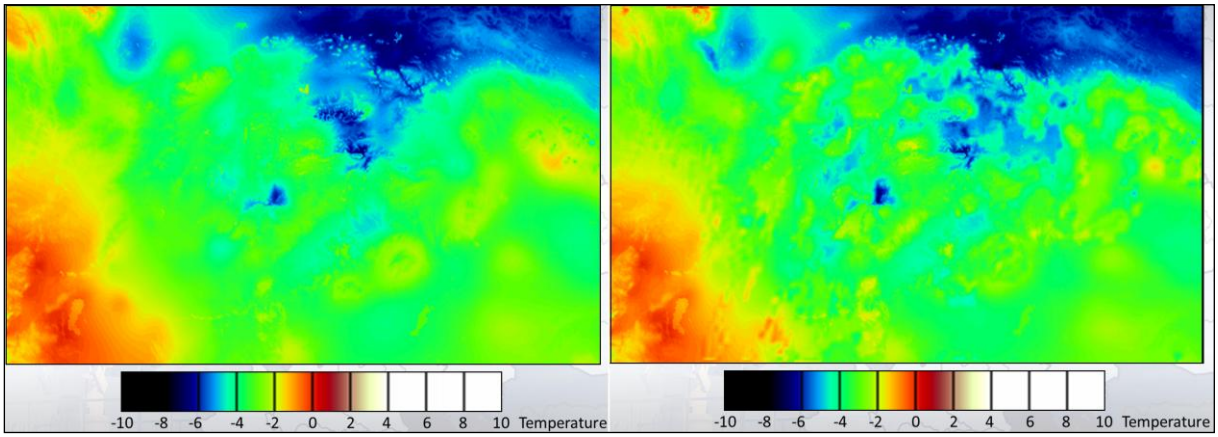

Figure 5.5 INCA-SK temperature fields (1km space resolution) calculated over Slovak domain. Before (left) and after (right) the correction applied. Method suppressed in this case ground station effects called bull-eyes typical for areas of low density of ground observations.

Correction of NWP temperature fields using satellite data is an example, how satellite data can improve numerical data and products used in nowcasting and weather forecasting. Satellite data can be used also for control of precipitation distribution over certain regions measured by conventional methods like raingauges and meteorological radars. These data cannot be replaced with satellite data, but satellite data can help to improve the quality of final product. Example of such improvement is shown in Fig. 5.6.

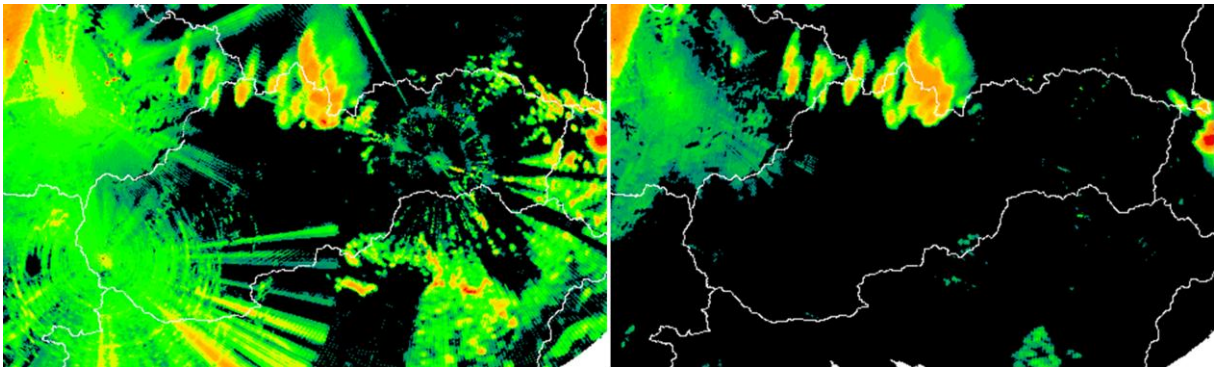

Figure 5.6 Comparison of daily precipitation fields from different data sources and quality settings created by the INCA system for the 2nd July 2012. Left panel shows only radar composite. Right panel shows final precipitation field including quality control by satellite NWCSAF products.

5.2 Project H-SAF of EUMETSAT – validation activities and first operational products

Validation activities of SHMÚ in H-SAF project, CDOP-2 phase started from the 1st March 2012 as the next 5 years period with continuous parallel development and operational production of products based on satellite data. Project is devoted to operational hydrology and water management.

SHMÚ contributed by development of common validation procedures for validation of precipitation products. Procedures were adopted by 6 European countries (Belgium, Germany, Hungary, Italy, Turkey and Slovakia) which use radar data as a ground truth to compare with satellite derived precipitation values. In total data from 59 C-band radars, which ensure wide area coverage with different orography and climate regimes, are used as input to this validation. Slovak experts exploited rich experience in bulk processing of data and helped to build up efficiency and very fast validation procedures. Validation is done on monthly base for at least one year of operationally generated satellite product. Statistical scores are than checked whether they reach user requirements. All validation results are put into tabular forms of reports which are regularly issued and reviewed by EUMETSAT Review Board. Review results are serving to developers of products as a feedback.

Case studies are important tool for validation of H-SAF products. In reported period SHMÚ produced 11 case studies for different precipitation products and oriented for different weather situations. Emphases were done to products based on microwave measurements, where proper up scaling of radar data to satellite field of view was developed. Example of downscaling is shown in Fig. 5.7. In case of severe convection studies show parallax shifts of cloud tops and measure of matching precipitation areas after the parallax corrections. In case of accumulated precipitation studies verified the amount of precipitation during extreme flood events.

Final utilization of H-SAF products is their assimilation into hydrological runoff models. While some products can be used simply as replacement of conventional ground data with satellite data (case of accumulated precipitation), other products must be assimilated in a special way. Soil moisture ground observations are very rare and therefore this parameter is often simulated inside

hydrological models. Simulated values can be replaced with satellite derived values, if they represent the same soil layer. SHMÚ proposed linear transformation of satellite soil moisture data in the first step. Satellite data from days without snow cover and no frosty days were taken into account. Synthetic time series of transformed soil moisture were calculated and used to update model parameters. Both variables (observed discharges and satellite derived soil moisture) were assigned by weights. Parameters of soil and runoff routines were slightly adjusted against more than one output variable. As output we received improved runoff over test river catchments (see Fig. 5.8).

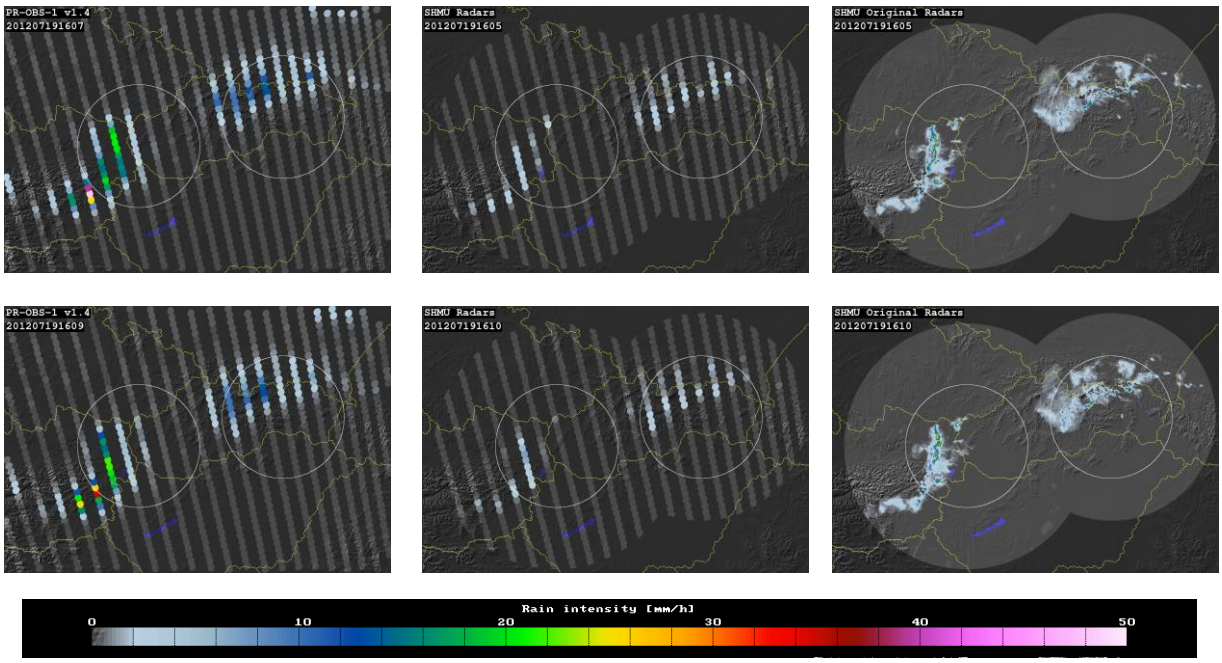

Figure 5.7 Instantaneous precipitation fields from 19 July 2012 observed by H01 product (left column), SHMU radar network upscaled to satellite grid (middle) and SHMU radar network in full resolution (right column) corresponding to DMSP17 overpass at 16:07 UTC (top row) and DMSP16 overpass at 16:09 UTC (bottom row). The precipitation values are shown as satellite IFOVs projected over the radar composite domain. White circles depict 120 km rain-effective range of the radars inside which data are compared.

Visual comparison of updated model outputs with observed and original simulated discharges show good agreement between time series. Especially recession part of flood wave in July, caused by convective precipitation, is simulated in accordance with observed discharge data. Problematic is winter season, when satellite soil moisture data are inaccurate due to frosty days and days with snow cover.

Soil moisture satellite product emerged as a promising input for multi-criteria update or calibration (against more than one output variable) of used rainfall-runoff model. It is important for reliable simulations of internal processes.

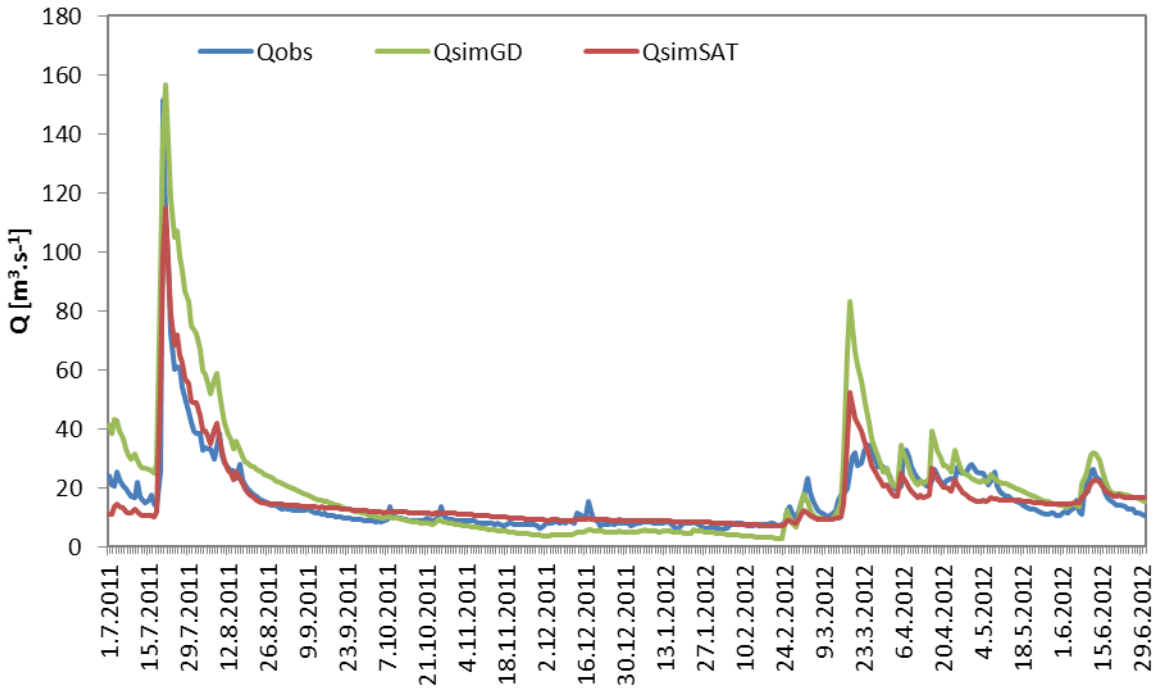

Figure 5.8 Comparison of observed runoff (Qobs, blue line) on the river Hron test basin against runoff simulated by ground data (green line) and against runoff simulated by satellite data (red line) for the period from July 2011 to June 2012.

5.3 Participation of SHMÚ in EUMETSAT Convection Working Group

The Convection Working Group (CWG) is an initiative of EUMETSAT and its member states, and the European Severe Storms Laboratory. The focus of this working group is to establish a comprehensive inventory of the available applications in severe storms detection and nowcasting, with the aim to get deeper insight into the differences and commonalities of the available techniques and products, and their specific areas of application.

One of important subjects studied in this field is detection of overshooting tops (OT). Overshooting tops are small-scale features atop storm clouds observed in high resolution satellite imagery. OT indicates the presence of a strong updraft of sufficient strength to penetrate through the tropopause and into the lower stratosphere. Severe weather and aviation turbulence often occur near the OT region. OT can be observed or inferred in visible and IR satellite imagery. Fine temporal ($\leq$ 5 min) and spatial resolution ($\leq$ 1 km) satellite imagery are needed to highlight important details on OT time evolution and updraft intensity. While polar orbiting satellites provide fine spatial resolution but coarse time resolution, geostationary satellites can provide sufficient time sampling of OT in rapid scan operations and, in general, are more suitable for continuous observation and detection of OT over wide regions.

Operational satellite-based cloud top height algorithms will often fail to assign representative heights to OT pixels because they are colder than any temperature represented in a nearby rawinsonde or NWP model profiles. The tropopause height is used as a default OT height when IR BT is lower than any temperature in the co-located profile. Knowledge of the OT height is very important to the aviation industry as pilots face the choice of whether to fly above or around an OT. Satellite-derived cloud heights are one of the few sources of observational guidance in many regions. The shadows cast by OT features upon the surrounding cirrus anvil cloud in low solar elevation angle conditions can be used to estimate the magnitude of OT penetration into the upper troposphere/lower stratosphere region, potentially serving as valuable guidance to the aviation community in the absence of reliable satellite-derived cloud top heights. Example of OT penetration height measurement is shown in Fig. 5.9.

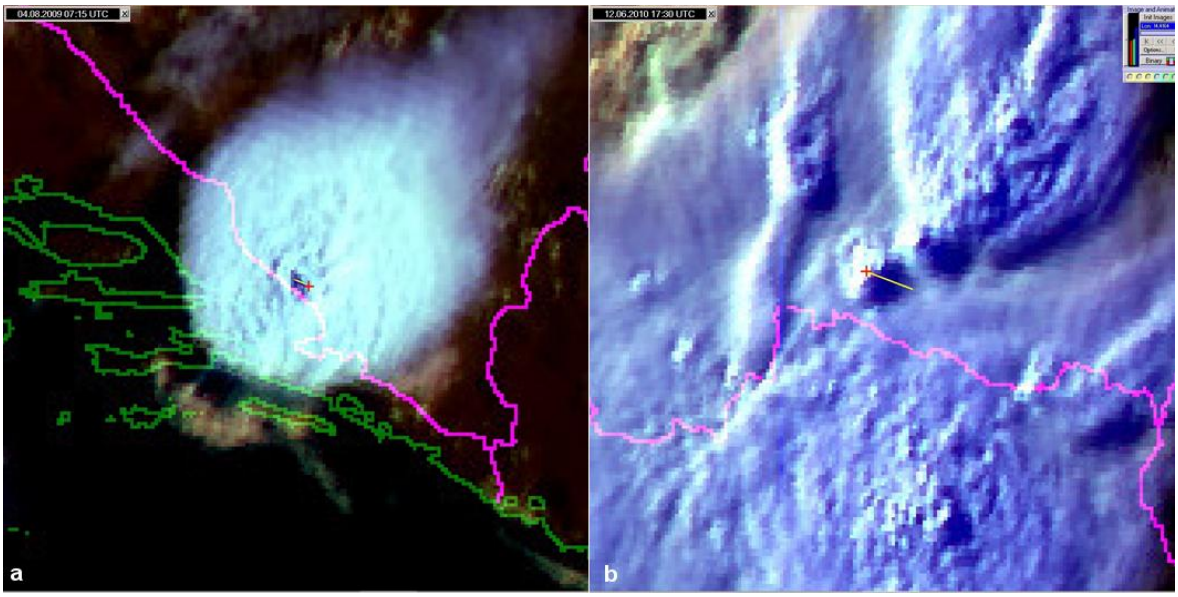

Figure 5.9. Example of OT penetration height measurement: a) Case 4th August 2009 07:15 UTC failed due to very high Sun elevation angle (38.5°). b) Case 12th June 2010 17:30 UTC, Sun elevation 10.6°, estimated OT height 2893m. Both cases were co-located with IR detection method. Red Cross indicates IR detection, yellow line length of the shadow.

The goal of our study was to utilize a combination of IR spatial gradients near OT signatures and the OT tropopause penetration magnitude observed by MSG SEVIRI to characterize the lapse rate associated with tropopause penetrating convection. It is the hope that cloud top height algorithm developers could use IR spatial gradients in combination with lapse rate information to assign heights that are more representative to OT.

We used significant dataset of OT, more than 20000 detections from IR and 5000 from HRV SEVIRI imagery with the aim to show whether OT penetration height is measurable by shadow technique and if some relations between IR BT and height parameters could be found. Using a trend line between OT penetration height and Minimum OT BT and Anvil BT difference, we derived possible lapse rate of OT cooling above the anvil level in interval (3 to 7.3 K/km), which is too low in comparison to generally valid values of wet lapse rate (5.46 K/km) and dry lapse rate (9.8 K/km). We assume that two factors – low IR resolution of SEVIRI imager and inability to detect very low OT by shadow technique are the reasons of bias for lapse rate derived from statistical

data set. The lapse rate becomes 9.1-9.4 K/km when the ~9 K warm bias induced by coarse geostationary imagery data is accounted for, suggesting that the HRV method is providing reasonable OT penetration heights.

This work was based only on 15-minute SEVIRI observations and it is not enough to estimate the sampling point in OT lifecycle. Rapid scan imagery with higher frequency (< 2.5 min from SEVIRI, 30 seconds from GOES-R ABI) can help to show where IR-Height relation for OTs starts to break down from adiabatic theory as OT warm via mixing with the stratospheric air.

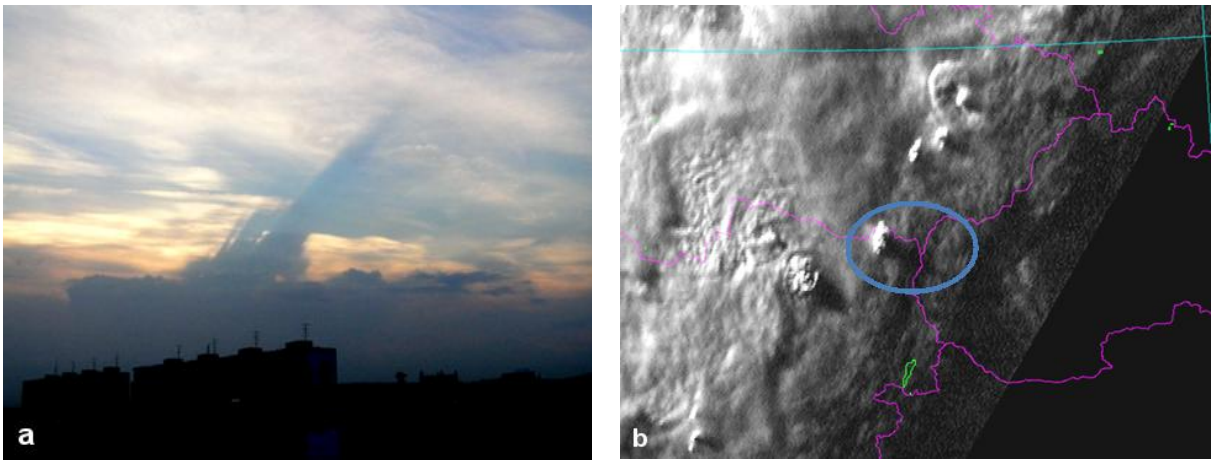

Figure 5.10 a) Photo of storm cloud from 30th May 2005 18:19 UTC with well-defined shadow of OT. b) MSG SEVIRI HRV channel satellite image from 30th May 2005 18:15 UTC. The storm shown in Fig. 5.10b is highlighted by blue circle.

The storm captured in the photo shown in Fig. 5.10a was located along the border between north Austria and south Moravia. A well-defined shadow was cast on cirrus clouds southeast of the storm core by an overshooting cloud top (OT). According to the satellite image (Fig. 5.10b) the storm was about 80 km to the NW of Bratislava.

The anvil BT distribution (Fig. 5.11a) shows that the HRV method (blue line) selects systematically colder anvils then IR method (red line), with a mean difference near 2 K. The OT BT distribution (Fig. 5.11b) shows that the HRV method (blue) selects systematically colder OTs then IR method (red), with a mean difference near 2 K. On average, the OT was 8 K colder than anvils regardless of method used to identify them: 220-212 = 218-210 = 8K.

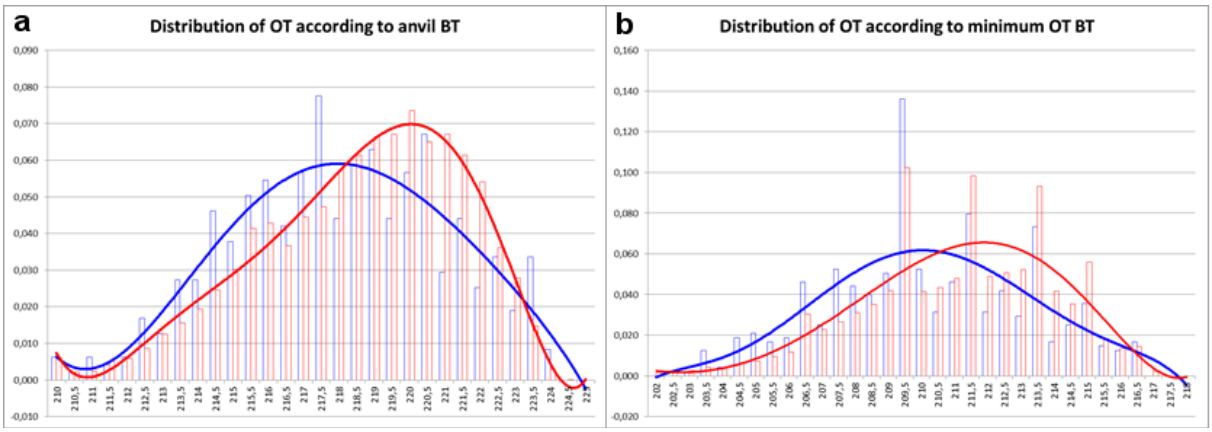

Figure 5.11 Relative frequency of anvil brightness temperatures (a) and Minimum OT brightness temperatures (b) for both detection methods (red line for IR, blue for HRV).

For a better understanding of the relations between anvils BT, OT BT and OT height, we created various distributions which are displayed in Fig. 5.12. From the relation between Min OT BT and Anvil BT (Fig. 5.12a) it is evident that colder anvils produce also colder OT. On average OT are 8 degrees colder than anvils. If we assume 9.8 K/km for dry adiabatic lapse rate, the mean OT penetration height based on IR BT imagery is 8 K / 9.8 K/km ~ 800m. If we consider wet adiabatic lapse rate value 5.5 K/km, the mean OT penetration height is ~1500 m.

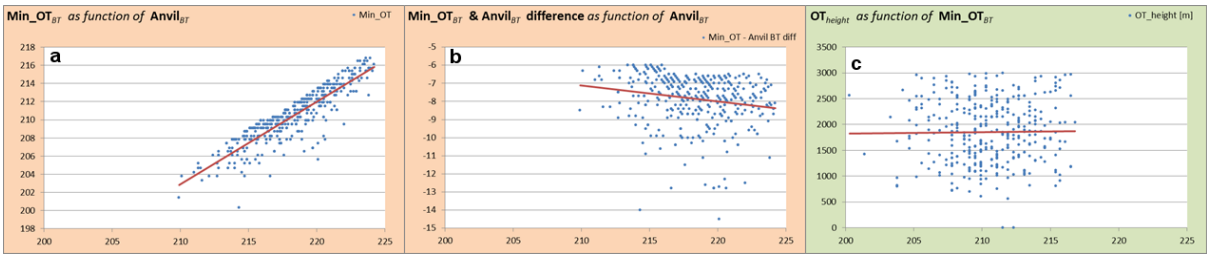

Figure 5.12 Relations between Minimum OT BT, anvil BT and OT height obtained from processed statistical data set.

The mean OT penetration height based on shadows from HRV imagery is 1800m as indicated by the distribution from Fig. 5.12c. We observe a noticeable bias varying from 335m (1800-1465) to 984m (=1800-816) between the IR and HRV methods. If we assume that cooling inside updrafts is somewhere between a wet and dry adiabatic process, it is necessary to explain the bias in OT height assignments. We assume three possible reasons of bias:

1. Missing detections of OT with penetration height <1000m by HRV method, (low OT is visible only when Sun elevation is equally low).
2. Subjective preference of higher OT cases in manual selection (well visible OT),
3. The relatively coarse 5 km MSG SEVIRI IR spatial resolution over Central Europe (areal averaging of BT by IR sensor and impossibility to measure very minimum cold spots of OT).

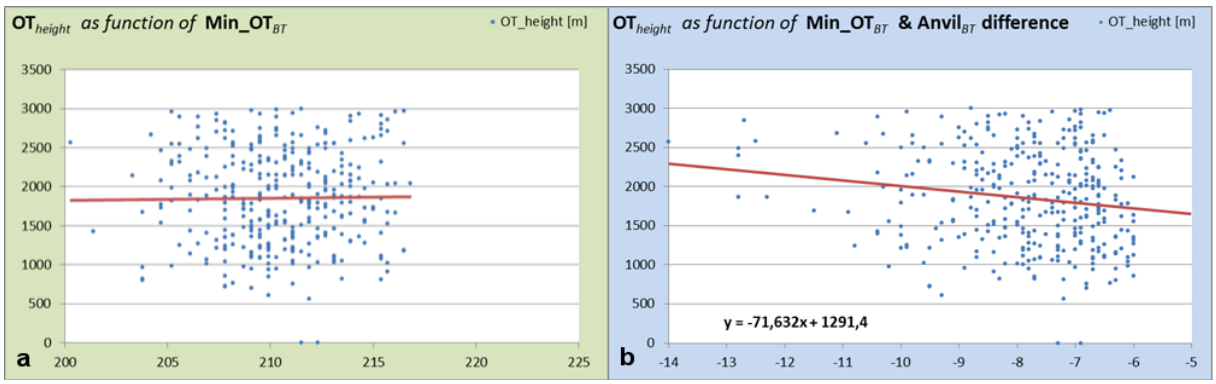

Figure 5.13: a) Constant distribution of OT height according Min OT BT. b) Gained using Min OT and anvil BT differences.

Finally, the statistical dataset shows that colder anvils produce not only colder but higher OT (see Fig. 5.13). While there is no any change of mean penetration height with observed minimum OT BT (Fig. 5.13a), we can find higher OT for higher BT differences between OT and anvil (Fig. 5.13b). For a -5 K difference, the mean OT penetration height is about 1600m, but for a -14K difference, the OT mean height reaches 2300m. This relation can be expressed by linear approximation y= -71.6x + 1291, where x is BT difference and y is averaged OT height. Consequently, we can use this approximation to calculate adiabatic cooling rate inside updrafts producing overshooting tops over the tropopause level (see Fig. 5.14).

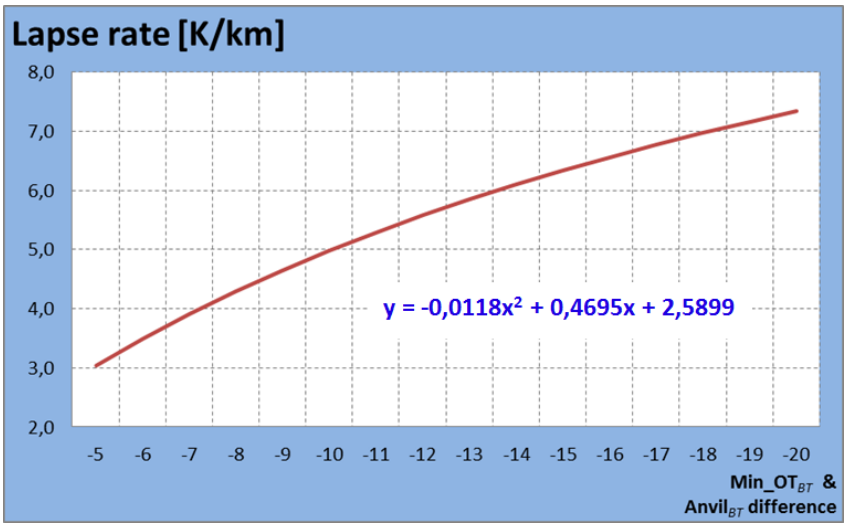

Figure 5.14 Adiabatic lapse rate calculated for Minimum OT BT and anvil BT differences in interval (-5; -20K) using linear approximation for height shown in Figure 5.13b.

References Remote Sensing and Space Meteorology:

(1, 2, 8, 9, 14, 17, and 18 in Slovak)

1. BARKA, I. - BETÁK, J. - BUCHA, T. - CEBECAUER, T. - FERANEC, J. - HAGUE IGONDOVÁ, M. - HEFTY, J. - HERDA, P. - HLAVÁČ, T. - HUSÁRIK, M. - JANÁK, J. - KAŇÁK, J. - KUDELA, K. - MIŠKOVÁ, M. - NOVÁČEK, J. - NOVÁKOVÁ, M. - SVIČEK, M. - SVOREŇ, J. - ŠÚRI, M. - TAKÁČ, J. (2012). Meniace sa Slovensko očami satelitov. Feranec, J. ed. Veda, Bratislava, DVD + 72 p. [in Slovak]
2. BUCHA, T. - BARKA, I. (2013). Postup rozpadu smrečín v období 2000–2012. In. Kunca, A. (ed.): zborník referátov z 22. ročníka medzinárodnej konferencie „Aktuálne problémy v ochrane lesa 2013“. NLC Zvolen, pp. 125–130 [in Slovak]
3. BUCHA, T. - SLÁVIK, M. (2013). Improved methods of classification of multispectral aerial photographs: evaluation of floodplain forests in the inundation area of the Danube. *Folia Forestalia Polonica*, series A, 55(2): 58–71.
4. FERANEC, J. - SOUKUP, T. (2013). Map presentation of changes in Europe´s artificial surfaces for the periods 1990-2000 and 2000-2006. Central European Journal of Geosciences, 5, 2, pp. 323-330.
5. FERANEC, J. - SOUKUP, T. - HAZEU, G. - JAFFRAIN, G. (2012). Land Cover and Its Change in Europe: 1990-2006. In Chandra, G. ed. Remote Sensing of Land Use and Land Cover: principles and applications. CRC Press, Boca Raton, pp. 285-301.
6. KAŇÁK, J., BEDKA, CH., SOKOL, A. (2012). Mature convective storms and their overshooting tops over Central Europe – overshooting top height analysis for summers 2009-2011. EUMETSAT Meteorological Satellite Conference, 3-7 September 2012, Sopot, Poland.
7. KOPECKÁ, M. - ROSINA, K. - RÁBEKOVÁ, A. (2012). Urban Expansion Mapping Based on VHR Satellite Imagery. In Bandrova, T., Konecny, M., Zhelezov, G. eds. 4th International Conference on Cartography and GIS, vol. 1. Bulgarian Cartographic Association, Sofia, pp. 237-246.

8. NOVÁKOVÁ, M. - SVIČEK, M. (2008). Implementation of European system for estimating yields and crop production (CGMS and MCYFS) in Slovakia. Final report. SSCRI Bratislava, 2008, 62 pp. [in Slovak]
9. NOVÁKOVÁ, M. - KLIKUŠOVSKÁ, Z. - SVIČEK, M. (2009). Completing and application of the National agro-meteorological modeling system for estimating yields and crop production (SK_CGMS). Final report. SSCRI Bratislava, 52 pp. [in Slovak]
10. NOVÁKOVÁ, M. - KLIKUŠOVSKÁ, Z. - SVIČEK, M. (2013). Application and updating of the National agro-meteorological modeling system for estimating yields and crop production (SK_CGMS). (in Slovak), Final report. SSCRI Bratislava, 69 pp.
11. RINOLLO, A., VULPIANI, G., PUCA, S., PAGLIARA, P., KAŇÁK, J., LÁBÓ, E., OKON, L., ROULIN, E., BAGUIS, P., CATTANI, E., LAVIOL, S., LEVIZZANI, V. (2013). Definition and impact of a quality index for radar-based reference measurements in the H-SAF precipitation product validation. Nat. Hazards Earth Syst. Sci., 13, 2695-2705, doi:10.5194/nhess-13-2695-2013.This work is distributed under the Creative Commons Attribution 3.0 License.
12. SAČKOV, I. - SMREČEK, R. - TUČEK, J. (2014). Forest transportation survey based on airborne laser scanning data and GIS analyses. GIScience & Remote Sensing. Accepted February 7. http://dx.doi.org/10.1080/15481603.2014.883213
13. SAČKOV, I. - KARDOŠ. M. (2014). Forest delineation based on LiDAR data and vertical accuracy of the terrain model in forest and non-forest area. Ann. For. Res. In print.
14. SLÁDEK, J. - RUSNÁK, M. (2013). Low-cost micro UAV technologies in geography (a new method of spatial data collection). Geographical Journal, 65, 3, pp. 269 – 285. [in Slovak]
15. SVIČEK, M., KOVÁČIKOVÁ, I. et al. (2012). The 2012 campaign of remote-sensing control of area-based subsidies. Final report, SSCRI Bratislava, 19 pp.

16. SVIČEK, M. - KOVÁČIKOVÁ, I. et al. (2013). The 2013 campaign of remote-sensing control of area-based subsidies. Final report, SSCRI Bratislava, 20 pp.

17. VLADOVIČ, J. - BUCHA, T. (2013). Inovatívne prístupy v mapovaní a posudzovaní štruktúry a textúry spoločenstiev a porastov v horských lesoch Nízkych Tatier. *Lesnícky časopis - Forestry Journal*, 59(1), 19–37. [in Slovak]

18. VLADOVIČ, J. - BUCHA T. - BARKA, I. et al. (2011). Štruktúra lesa – inovatívne prístupy v tematickom mapovaní a klasifikácii. s. 37–95. In. Vladovič, J., (ed.): Štruktúra a diverzita lesných ekosystémov na Slovensku. NLC Zvolen, 252 pp. [in Slovak]

6. Institutions involved in Space Research relevant to COSPAR.

Members of the National Committee of COSPAR with e-mail addresses. The website of NC is *http://nccospar.saske.sk*.

Astronomical Institute (AI)
Slovak Academy of Sciences (SAS)
Stará Lesná
059 60 Tatranská Lomnica
J. Rybák (choc@astro.ta3.sk, NC member)

Faculty of Mathematics, Physics and Informatics (FMPI)
Comenius University
Mlynská dolina
842 15 Bratislava
J. Masarik (Jozef.Masarik@fmph.uniba.sk, NC member)

National Forest Centre
T.G. Masaryka 22
960 92 Zvolen
contact: T. Bucha (bucha@nlcsk.org)

Geophysical Institute (GI)
Slovak Academy of Sciences (SAS)
Dúbravská cesta
842 28 Bratislava
M. Revallo (milos.revallo@savba.sk, Secretary of NC)

Institute of Animal Biochemistry and Genetics
Slovak Academy of Sciences (SAS)
Moyzesova 61
900 28 Ivanka pri Dunaji
I. Hapala (Ivan.Hapala@savba.sk, NC member)

Institute of Experimental Endocrinology (IEE)
Slovak Academy of Sciences (SAS)
Vlárska 3
833 06 Bratislava
R. Kvetňanský (ueenkvet@savba.sk, Vice- chair of NC)

Institute of Experimental Physics (IEP)
Slovak Academy of Sciences (SAS)
Watsonova 47
040 01 Košice
K. Kudela (kkudela@kosice.upjs.sk, Chair of NC, Representative of Slovak NC to COSPAR)

Institute of Geography (IGG)
Slovak Academy of Sciences (SAS)
Štefánikova 49
814 73 Bratislava
J. Feranec (feranec@savba.sk, NC member)

Institute of Materials and Machine Mechanics
Slovak Academy of Sciences (SAS)
Račianska 75
831 02 Bratislava 3
J. Lapin (ummslapi@savba.sk, lapin@up.upsav.sk, NC member)

Institute of Measurement Science (IMS)
Slovak Academy of Sciences (SAS)
Dúbravská 9
842 19 Bratislava
contact: I. Frollo (frollo@savba.sk)

Institute of Normal and Pathological Physiology (INPP)
Slovak Academy of Sciences (SAS)
Sienkiewiczova 1
813 71 Bratislava
contact: F. Hlavačka (Frantisek.Hlavacka@savba.sk)

Slovak Central Observatory (SCO)
Komárňanská 134
947 01 Hurbanovo
contact: Ivan Dorotovič (ivan.dorotovic@suh.sk)

Slovak Environmental Agency
Remote Sensing Department
Tajovského 28
975 90 Banská Bystrica
contact: N. Machková (machkova@sazp.sk)

Slovak Hydrometeorological Institute
Maly Javornik Observatory
827 13 Bratislava
D. Kotláriková (dagmar.kotlarikova@shm.sk, NC member)

Soil Science and Conservation Research Institute
Gagarinova 10
827 13 Bratislava
contact: M. Sviček (svicek@vupu.sk)

Space Research in Slovakia 2012 – 2013
National Committee of COSPAR in Slovak Republic
Slovak Academy of Sciences
Institute of Experimental Physics, SAS, Košice

Editors: Karel Kudela and Ján Feranec
Technical editor: Jana Štetiarová

Printed by CopyCenter Košice, May 2014
ISBN 978-80-89656-07-3